



HAL
open science

Energetic upscaling strategy for grain growth. I: Fast mesoscopic model based on dissipation

Sofia Sakout, Daniel Weisz-Patrault, Alain Ehlacher

► To cite this version:

Sofia Sakout, Daniel Weisz-Patrault, Alain Ehlacher. Energetic upscaling strategy for grain growth. I: Fast mesoscopic model based on dissipation. *Acta Materialia*, 2020, 196, pp.261-279. 10.1016/j.actamat.2020.06.032 . hal-03042522

HAL Id: hal-03042522

<https://hal.science/hal-03042522v1>

Submitted on 6 Dec 2020

HAL is a multi-disciplinary open access archive for the deposit and dissemination of scientific research documents, whether they are published or not. The documents may come from teaching and research institutions in France or abroad, or from public or private research centers.

L'archive ouverte pluridisciplinaire **HAL**, est destinée au dépôt et à la diffusion de documents scientifiques de niveau recherche, publiés ou non, émanant des établissements d'enseignement et de recherche français ou étrangers, des laboratoires publics ou privés.

Energetic upscaling strategy for grain growth. I: Fast mesoscopic model based on dissipation.

Sofia Sakout^{a,b}, Daniel Weisz-Patrault^{a,*}, Alain Ehrlicher^b

^aLMS, CNRS, École Polytechnique, Institut Polytechnique de Paris, F-91128 Palaiseau, France

^bLaboratoire Navier, CNRS, École Ponts ParisTech, 6 & 8 Ave Blaise Pascal, F-77455 Marne La Vallée, France

Abstract

Tailoring microstructures by optimizing fabrication or forming processes is a challenge for metal industries. However, predicting microstructure evolution implies to develop models at the scale of the polycrystal, which is incompatible with large scale simulations of processes. In this context, we propose an energetic upscaling strategy to model anisotropic grain growth at large scale without losing detailed grains statistics. Thus, a fast mesoscopic model is necessary to establish a large database of computations in order to develop a macroscopic model whose state variables contain statistical descriptors of the microstructure. This paper focuses on a fast mesoscopic model based on Voronoi-Laguerre tessellations, which are updated at each time step to capture grain growth. Several energetic contributions are considered at different scales. The grain boundary energy is obtained as a function of misorientation from molecular dynamics, and the dissipated power is obtained from crystal plasticity theory. The evolution law at the mesoscopic scale is obtained by considering all energetic contributions in the representative volume element, and from thermodynamic laws and approximate mass conservation. This upscaling approach reaches short computation time, which is essential to establish the database underlying the macroscopic model. Basic grain statistics are validated by comparison to classical models. Moreover, a good agreement is observed with an experiment conducted on pure iron. The model is then used to analyze the evolution of detailed statistics. To capture grain growth at macroscopic scale, it is necessary to consider couplings between means and standard deviations of various distributions (e.g., size, shape, misorientation etc.)

Keywords: Grain growth, Upscaling, Anisotropic grain boundary energy, Dissipated power, Voronoi-Laguerre tessellation

1. Introduction

Grain growth is a thermally activated mechanism that usually occurs after recrystallization during annealing of metals. During grain growth some grains grow at the expense of other grains depending of their respective sizes and crystallographic orientations, which leads to grain coarsening [1]. Classical statistical descriptors of the polycrystalline structure such as morphological and crystallographic textures (e.g., grain size, shape and crystal orientation distributions) evolve during the process. Thus, for different fabrication or forming processes, temperature conditions could be optimized to obtain targeted microstructures, especially for

*Corresponding author: daniel.weisz-patrault@polytechnique.edu

large heterogeneous parts. However, mechanisms involved during grain growth arise at the scale of grain boundaries (GB). Thus, numerical simulations of texture evolution may be difficult for macroscopic parts, which hinders the development of optimization loops to adjust process parameters.

Thus, this paper and the subsequent paper [2] aim at developing an upscaling strategy to establish a macroscopic model of grain growth that fully relies on finer scales and whose state variables contain statistical descriptors of the grain structure. The proposed upscaling strategy involves considering grain growth at various scales. As shown in figure 1, four typical scales are distinguished in this paper: (i) the atomic scale (e.g., crystal lattice and interatomic potential), (ii) the microscopic scale (e.g., grain boundaries), (iii) the mesoscopic scale (e.g., polycrystalline structure) and (iv) the macroscopic scale (statistical descriptors of the grain structure). As energetic concepts are valid at all scales, the upscaling strategy fundamentally relies on various energetic contributions arising at different scales. This energetic upscaling strategy is developed within the framework of standard generalized media [3] that are characterized by their *free energy* and *dissipated power*. These two potentials arise in the energy balance equation combining the first and second laws of thermodynamics, and they depend on macroscopic state variables that should be defined so that the macroscopic state statistically represents the grain structure. The determination of the macroscopic free energy and dissipation potentials as a function of the state variables enables to establish the evolution law of the system at the macroscopic scale. The proposed upscaling strategy consists in determining these two potentials not axiomatically (with parametric functions and calibration with experiments), but on a more physical basis by using a large *database* of computations carried out at the mesoscopic scale. Thus, the macroscopic model emerges from finer scales and is compatible with thermodynamics.

It should be noted that we do not propose a multiscale approach, for which simulations at the mesoscopic scale are performed online during the macroscopic computation. On the contrary, all the computations at the mesoscopic scale are performed in advance and stored in the database probing the space of polycrystalline structures. On this basis, we can identify the macroscopic free energy and dissipated power as a function of the macroscopic state variables in order to obtain an evolution law that accounts for statistical descriptors of the grain structure.

Therefore, the database requires to use intensively a mesoscopic model of grain growth. As a consequence, a sufficiently fast mesoscopic model should be established. This paper specifically focuses on this aspect, whereas the identification of the macroscopic model will be broached in [2]. Many different approaches have been proposed to model grain growth at the mesoscopic scale (e.g., see [1, 4] for reviews). Most of them rely on the classical curvature driven GB motion evolution law:

$$v_{CD} = m_{CD} \gamma \kappa \quad (1)$$

where v_{CD} is the inward speed of the GB (where CD stands for *curvature driven*), m_{CD} is the mobility ($\text{m}^4 \cdot \text{J}^{-1} \cdot \text{s}^{-1}$), γ is the surface energy ($\text{J} \cdot \text{m}^{-2}$) and κ is the grain curvature. Since this evolution law holds at the scale of the GB, many numerical approaches enable to refine the geometrical description of GBs in order to capture accurately GB motion. For instance, models based on cellular automaton and Monte Carlo method [5–9], mobile finite element modeling [10, 11], level set functions [12–14], phase field [15–20] or molecular dynamics [21–23] have been proposed. All these approaches produce very interesting results. However, the computational cost is usually incompatible with an intensive use as suggested within the proposed framework.

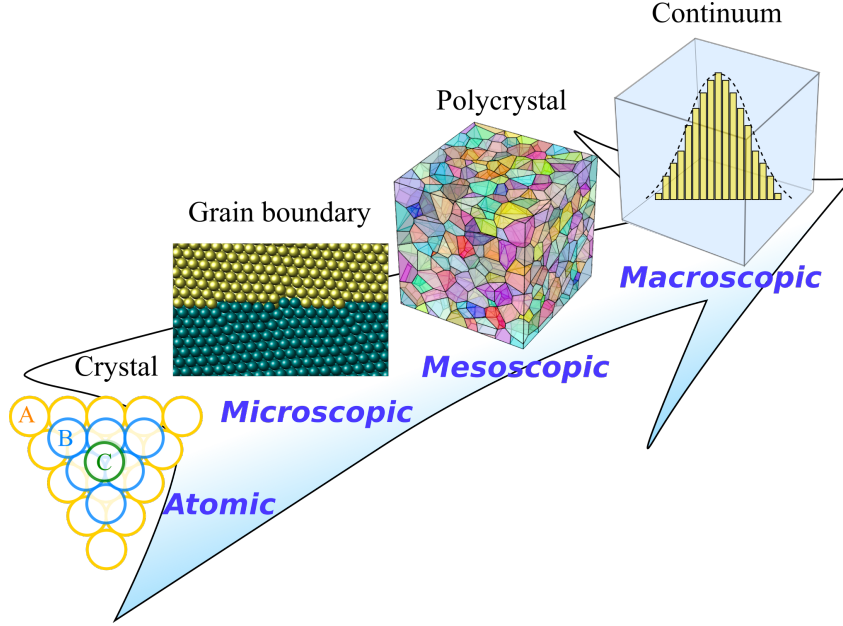


Figure 1: Different scales involved in the upscaling strategy

Other approaches reaching shorter computation time have also been proposed. For instance, vertex methods [24–27] consist in establishing the evolution law directly at the triple junctions and are relatively simple in two dimensions. However, the extension in three dimensions is difficult [1]. More recently, a fast mesoscopic model called *Orientated Tessellation Updating Method* (OTUM) has been proposed [28], and fully relies on Voronoi-Laguerre tessellation techniques that are usually used to approximate polycrystals at the mesoscopic scale. Very efficient algorithms have been developed with the possibility of controlling statistical distributions of grain size and shape (e.g., using the free software NEPER [29]). Crystal lattice orientation can also be specified for each grain, and the tessellation equipped with such an orientation field is called an *Orientated Tessellation* (OT). One can approximate the real evolution of the mesostructure as a succession of OT approximations. OTUM relies on the idea that the evolution law of the mesostructure can be formulated directly by modifying the parameters defining the OT. To the best of the authors knowledge this idea of updating Voronoi-Laguerre tessellation parameters to model grain growth has been proposed for the first times in [30, 31]. However, the evolution laws proposed in [30, 31] are questionable. Indeed, they are postulated to directly mimic the curvature driven evolution law (1) despite the fact that GBs have no curvature in a Voronoi-Laguerre tessellation. More importantly, the modification of a single parameter of the OT affects several GBs according to the Voronoi-Laguerre definition, which plays the role of a geometrical constraint on possible GB motions. Thus, the curvature driven evolution law (1) is not appropriate within the framework of OTUM, as it would necessitate to control GBs independently.

That is why in this paper, the evolution law is formulated at the mesoscopic scale (i.e., for the entire tessellation instead of each GB taken individually). Different energetic contributions are considered so that the evolution law relies on a physically consistent basis. More precisely, the evolution law is obtained through the energy balance equation at the mesoscopic scale, by specifying mechanisms at the microscopic scale: (i) the anisotropic GB energy and (ii) the dissipated power through any GB virtual motion. The proposed energetic framework enables to

consider not only the driving force (associated to the GB energy) but also the dissipated power as a resistive mechanism. The GB energy is estimated as a function of misorientation by molecular dynamics computations at the atomic scale. In addition, the dissipated power associated to GB motion is estimated by crystal plasticity for very low angle boundaries and atomic jumps and atomic diffusion are considered for high and intermediate angle boundaries respectively. Thus, a substantial link is made in this paper between atomic, microscopic and mesoscopic scales to derive the model. The final step enabling to extend this energetic upscaling to the macroscopic scale is not detailed in this paper but will be broached in [2].

From the macroscopic point of view, all the mesoscopic structures play the role of representative volume elements (RVE). This implies that each mesostructure is supposed to be extracted from a much larger polycrystalline structure. As a result, boundary conditions should be applied to the RVE to take into account interactions between the RVE and the rest of the polycrystal. This is achieved by defining the RVE as a subset of grains extracted from a larger OT, so that misorientations are affected to GBs at the edges of the RVE.

In addition, the set of possible OTs is a high dimensional vector space. Thus, the *database* should contain various RVEs sufficiently different from each other to probe efficiently the space of possible OTs. However, as detailed in the following, if crystal orientations are assigned purely randomly, then boundary misorientation distributions (BMD) are likely to be very similar to each other instead of spreading in the entire space of possible distributions. To overcome this difficulty, crystal orientations are assigned according to a specific procedure in order to match prescribed BMDs.

For the sake of simplicity, the proposed upscaling methodology is derived for plane hexagonal polycrystals. In 3D, this would correspond to face-centered cubic (fcc) crystals, and for each grain the direction $[111]$ is assumed to be aligned with the out of plane direction. Thus, there are three plastic slip systems in 2D, as shown in figure 2. Misorientation between two neighboring grains (characterized by five parameters in 3D) is characterized only by two parameters in 2D: the misorientation angle (denoted by $\Delta\theta$) and the orientation of the grain boundary plane (denoted by φ). Thus, the grain boundary energy considered in this paper is computed from fcc crystals sharing the same orientation $\langle 111 \rangle$ (tilt boundaries). The plane assumption enables to deal with thin structures such as thin films. In addition, since there are 3 plastic slip systems in the plane, the proposed approach also enables to reasonably approximate 3D structures.

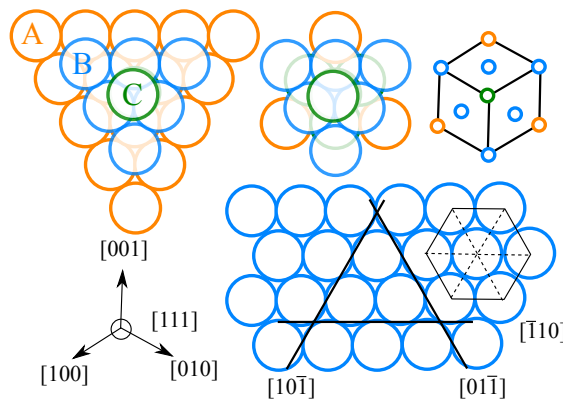


Figure 2: FCC crystal and (111) plane with plastic slip directions

The paper is organized as follows. General principles of OTUM are presented in section 2. In section 3 we detail the procedure enabling to generate different RVEs to probe the space of possible OTs. Mass conservation issues and the minimum number of grains that should be considered for the RVEs is discussed in section 4. Mechanisms at the microscopic scale are broached in section 5. In particular molecular dynamics computations are performed to obtain the GB energy, and the mobility is derived as function of misorientation. The mesoscopic evolution law, which constitutes the core equation of the model is derived in section 6. Results and discussion are provided in section 7. Classical models (Hillert distribution [32, 33] and von Neumann-Mullins law [34, 35]) are compared to the model to validate basic grain statistics. A comparison with an experimental study conducted on pure iron [36] is also presented and good agreement is observed. More detailed statistics are also analyzed to determine meaningful information to be considered at the macroscopic scale. Conclusive remarks are given in section 8.

2. Orientated Tessellation Updating Method

In this section mathematical definition of the OT is provided as well as general principles of the OTUM. A Voronoi-Laguerre tessellation is defined by N seeds whose dimensionless Cartesian coordinates are denoted by $(x_j, y_j) \in [0, 1]^2$ and N dimensionless weights denoted by $w_j \in \mathbb{R}_+$ (where $1 \leq j \leq N$). The tessellation is completely determined by the parameter vectors $\mathbf{x} = (x_1, \dots, x_N)$, $\mathbf{y} = (y_1, \dots, y_N)$, $\mathbf{w} = (w_1, \dots, w_N)$. Each cell (or grain) denoted by C_j (where $1 \leq j \leq N$) is defined as follows:

$$C_j = \left\{ \begin{pmatrix} x \\ y \end{pmatrix} \in \mathbb{R}^2, \forall k \in \{1, \dots, N\}, \left\| \begin{pmatrix} x - x_j \\ y - y_j \end{pmatrix} \right\|^2 - w_j \leq \left\| \begin{pmatrix} x - x_k \\ y - y_k \end{pmatrix} \right\|^2 - w_k \right\} \quad (2)$$

It is clear from the definition (2) that weights are defined up to a constant. Thus, the following constraint is added to obtain a univocal definition:

$$\sum_{j=1}^N w_j = 1 \quad (3)$$

Thus, weights \mathbf{w} lie in an affine hyperplane of dimension $N - 1$ and denoted by $P_a^{(N-1)}$, whose support is the hyperplane denoted by $P^{(N-1)}$ and:

$$\begin{cases} P^{(N-1)} = \{ \mathbf{w} \in \mathbb{R}_+^N, \mathbf{w} \cdot \mathbf{1} = 0 \} \\ P_a^{(N-1)} = \{ \mathbf{w} \in \mathbb{R}_+^N, \mathbf{w} \cdot \mathbf{1} = 1 \} = P^{(N-1)} + \mathbf{w}_0 \end{cases} \quad (4)$$

where $\mathbf{1} = (1, \dots, 1) \in \mathbb{R}^N$ and $\mathbf{w}_0 \in \mathbb{R}_+^N$ verifies $\mathbf{w}_0 \cdot \mathbf{1} = 1$. In addition, it should be noted that a cell C_j may be empty as shown in figure 3a. This property will be intensively used as some grains should disappear during grain growth. In 2D, crystallographic orientations are defined as N additional angles denoted by θ_j (where $1 \leq j \leq N$). In this paper, θ_j represent the $\langle 111 \rangle$ tilt angles. Thus, the OT tessellation definition necessitates the additional vector $\boldsymbol{\theta} = (\theta_1, \dots, \theta_N)$. Since the crystal lattice is plane hexagonal $\theta_j \in [0, \pi/3]$ (where $1 \leq j \leq N$). Therefore, the parameter set \mathcal{P}_{OT} defining OTs reads:

$$\mathcal{P}_{\text{OT}} = \left\{ \boldsymbol{\alpha} = (\mathbf{x}, \mathbf{y}, \mathbf{w}, \boldsymbol{\theta}) \in [0, 1]^N \times [0, 1]^N \times P_a^{(N-1)} \times \left[0, \frac{\pi}{3} \right]^N \right\} \quad (5)$$

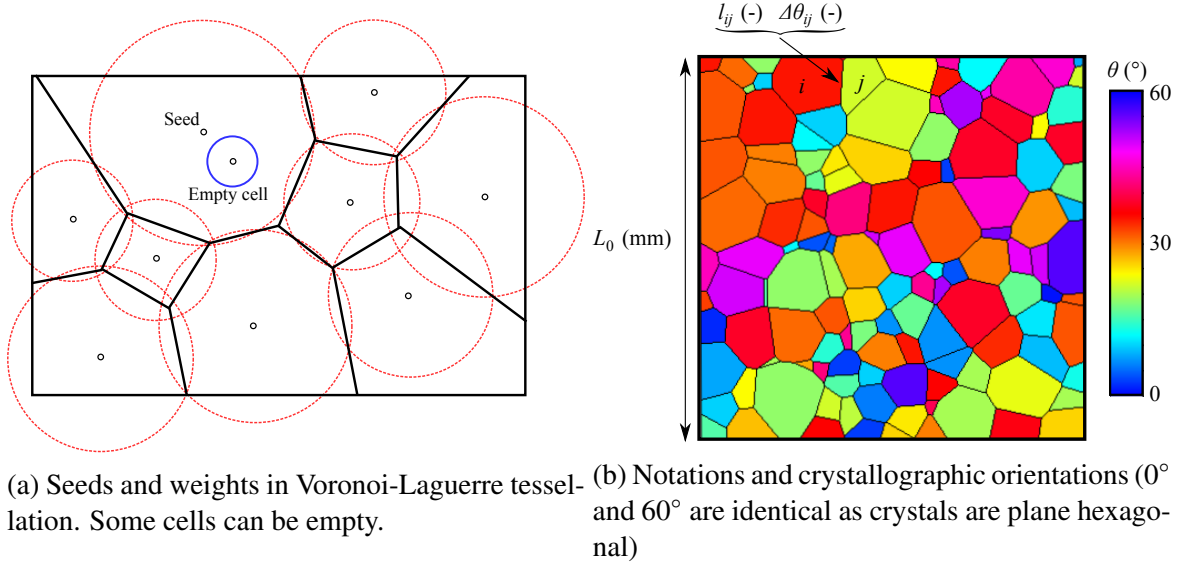


Figure 3: Orientated tessellation

Grain boundaries are indexed by pairs (i, j) where i and j denote two neighboring grains (where $1 \leq i \leq N$ and $1 \leq j \leq N$). The set of pairs of neighboring grains defining grain boundaries is denoted by I_{GB} :

$$I_{GB} = \{(i, j) \in \{1, \dots, N\}^2, j > i, C_i \cap C_j \neq \emptyset\} \quad (6)$$

The condition $j > i$ is meant to count each grain boundary only once. Since the parameters defining OTs are dimensionless, the physical size of the OT is given by L_0 representing the length of the box side in which the OT is contained, as shown in figure 3b. Moreover for any grain boundary $(i, j) \in I_{GB}$ (with i and j two neighboring grains) $l_{ij} \in [0, 1]$ denotes the dimensionless GB length and $\Delta\theta_{ij} = |\theta_j - \theta_i| \in [0, \pi/3]$ is the misorientation angle.

The general principle of the OTUM is to establish an evolution law directly on the parameter of the OT, that is to say that for $\alpha \in \mathcal{P}_{OT}$:

$$\dot{\alpha} = f(\alpha) \quad (7)$$

For the sake of simplicity we assume that only weights \mathbf{w} can evolve. In particular, θ is fixed. This implies that we neglect crystallographic rotations (obtained by activation of plastic slips systems in the bulk), which only affects the smallest grains [23]. Thus, the general evolution law reads for $\alpha = (\mathbf{x}, \mathbf{y}, \mathbf{w}, \theta) \in \mathcal{P}_{OT}$:

$$\dot{\mathbf{w}} = f(\alpha) \quad (8)$$

An explicit form of the evolution law (8) is derived in section 6.

3. Probabilistic procedure for orientation assignment

As mentioned in the introduction, the proposed energetic upscaling strategy necessitates to probe the space of possible OTs. Indeed, very different morphological and crystallographic textures may be observed [1] depending on fabrication and forming processes that impose specific temperature paths and deformation mechanisms.

The morphological texture is controlled by seeds (x, y) and weights w , whereas the crystallographic texture is controlled by the orientations θ . Morphology (e.g., shape and size distributions) may be controlled by optimization techniques in the free software NEPER [29]. In addition, one can generate tessellations by choosing x, y, w randomly (with various probability density functions), which enables to produce a *database* of very different tessellations with respect to sphericity and size distributions.

Since GB energy significantly depends on misorientation, the boundary misorientation distribution (BMD) (i.e., misorientations between neighboring grains) is essential for predicting anisotropic grain growth. Misorientation angles are simply deduced from crystal orientations but cannot be directly prescribed as a control parameter of the OT. Moreover, one cannot probe the space of possible BMDs by assigning crystal orientations purely randomly. Indeed, misorientations not only depend on crystal orientations but also on the network connectivity formed by the grains. In other words, the way to assign an orientation to a grain should depend on the orientation of its neighbors. If crystal orientations are assigned randomly in the OT (even considering various probability density functions) a statistical effect arises: small misorientations are favored¹. Thus, BMDs obtained with this method are very likely to be similar. That is why we need a specific procedure assigning crystal orientations in order to obtain various prescribed BMDs so that the space of possible BMDs can be explored efficiently. A Monte-Carlo optimization technique has been proposed in [38] and a rank optimization has been developed in [39]. However, optimization necessitates to re-assign several times orientations until the BMD matches the prescribed distribution, which is time consuming. As a large *database* is aimed, an alternative approach reaching very short computation time has been developed.

A stochastic step by step procedure is proposed for the orientation assignment (see figure 4). The target BMD is defined by a probability density function denoted by $p(\Delta\theta)$. The procedure is as follows. An initial grain is selected randomly and the orientation is arbitrarily set to θ_0 (in practice $\theta_0 = 0$). Then, one neighbor is selected, and its orientation θ_1 is assigned randomly as a draw of $p(\Delta\theta_{01})$. Indeed, θ_0 being already assigned, the probability of θ_1 is conditional to θ_0 , and reads as the probability of the misorientation angle $\Delta\theta_{01} = |\theta_1 - \theta_0|$. More formally, this reads:

$$p(\theta|\theta_0) = p(\Delta\theta_{01}) \quad (9)$$

where $p(\theta|\theta_0)$ is the probability density for θ_1 under the condition that θ_0 has already been assigned. This procedure is repeated to another neighbor etc. At some point, the selected grain denoted by i have several already assigned neighbors denoted by j_1, \dots, j_k , whose orientations are denoted by $\theta_{j_1}, \dots, \theta_{j_k}$ (see figure 4). Therefore, the orientation θ_i is determined as a draw of the following conditional probability density function:

$$p(\theta|\theta_{j_1}, \dots, \theta_{j_k}) = p(\Delta\theta_{ij_1}, \dots, \Delta\theta_{ij_k}) \quad (10)$$

where $p(\theta|\theta_{j_1}, \dots, \theta_{j_k})$ is the probability density for θ_i under the condition that $\theta_{j_1}, \dots, \theta_{j_k}$ have already been assigned, $\Delta\theta_{ij_1}, \dots, \Delta\theta_{ij_k}$ are the misorientation angles between the grain i and j_1, \dots, j_k respectively, and $p(\Delta\theta_{ij_1}, \dots, \Delta\theta_{ij_k})$ is the joint probability of misorientation. For the sake of simplicity, it is assumed that grain boundary misorientations are independent,

¹In 3D, uniform random orientation distribution classically leads to the Mackenzie disorientation distribution [37], which is not obtained in 2D. Indeed, plane hexagonal polycrystals correspond in 3D to fcc grains with the $\langle 111 \rangle$ direction aligned with the out of plane direction, which is a strong non-random texture.

hence:

$$p(\theta | \theta_{j_1}, \dots, \theta_{j_k}) = \prod_{m=1}^k p(\Delta\theta_{i_{j_m}}) \quad (11)$$

This process is repeated until all grain orientations have been assigned, as shown in figure 4. This probabilistic procedure is very fast but not exact. However, the obtained BMD is suf-

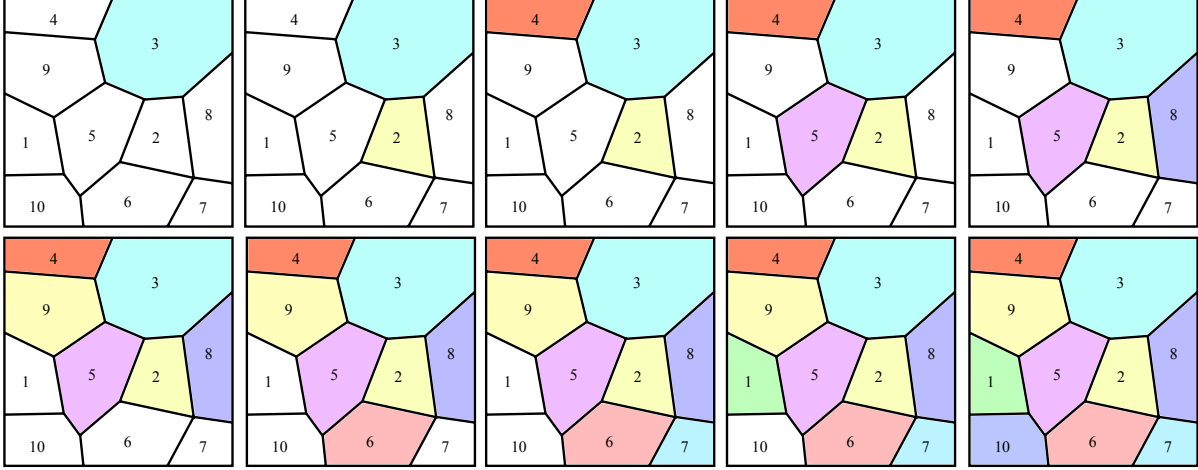


Figure 4: Principle of probabilistic orientation assignment

ficiently close to the target BMD to enable an efficient exploration of possible BMDs. For instance several orientations are assigned to the same Voronoi-Laguerre tessellation in figure 5. The obtained BMD is presented with histograms and the targeted BMD is presented in solid line. These examples have been generated with beta probability density $\mathcal{B}(\alpha, \beta)$ for the targeted BMD with parameters $\alpha = 1, 2$ and $\beta = 2, 3, 4$.

4. Representative volume element and mass conservation

The proposed mesoscopic model is meant to be used in an upscaling strategy. Thus, the mesoscopic evolution law should not be derived for an entire polycrystalline structure containing all the grains of the macroscopic object. Instead, the mesoscopic model should be derived for RVEs supposed to be embedded in a much larger polycrystalline structure. As a result, boundary conditions should be applied to the RVE to take into account interactions with the rest of the polycrystal. Boundary conditions consist of misorientations at the boundaries of the RVE. This section deals with the definition of RVEs and difficulties related to mass conservation.

4.1. Boundary conditions

A simple way to define the RVE is to generate an OT containing N grains and to consider a subset of n connected grains (with $n < N$) among the N grains and not belonging to the edges of the OT. Thus, all GBs in the RVE, including boundaries of the RVE, have a misorientation angle (see figure 6). Hence, boundary conditions are naturally defined. The evolution of the RVE is obtained by updating only the parameters of the n connected grains, while the parameters of

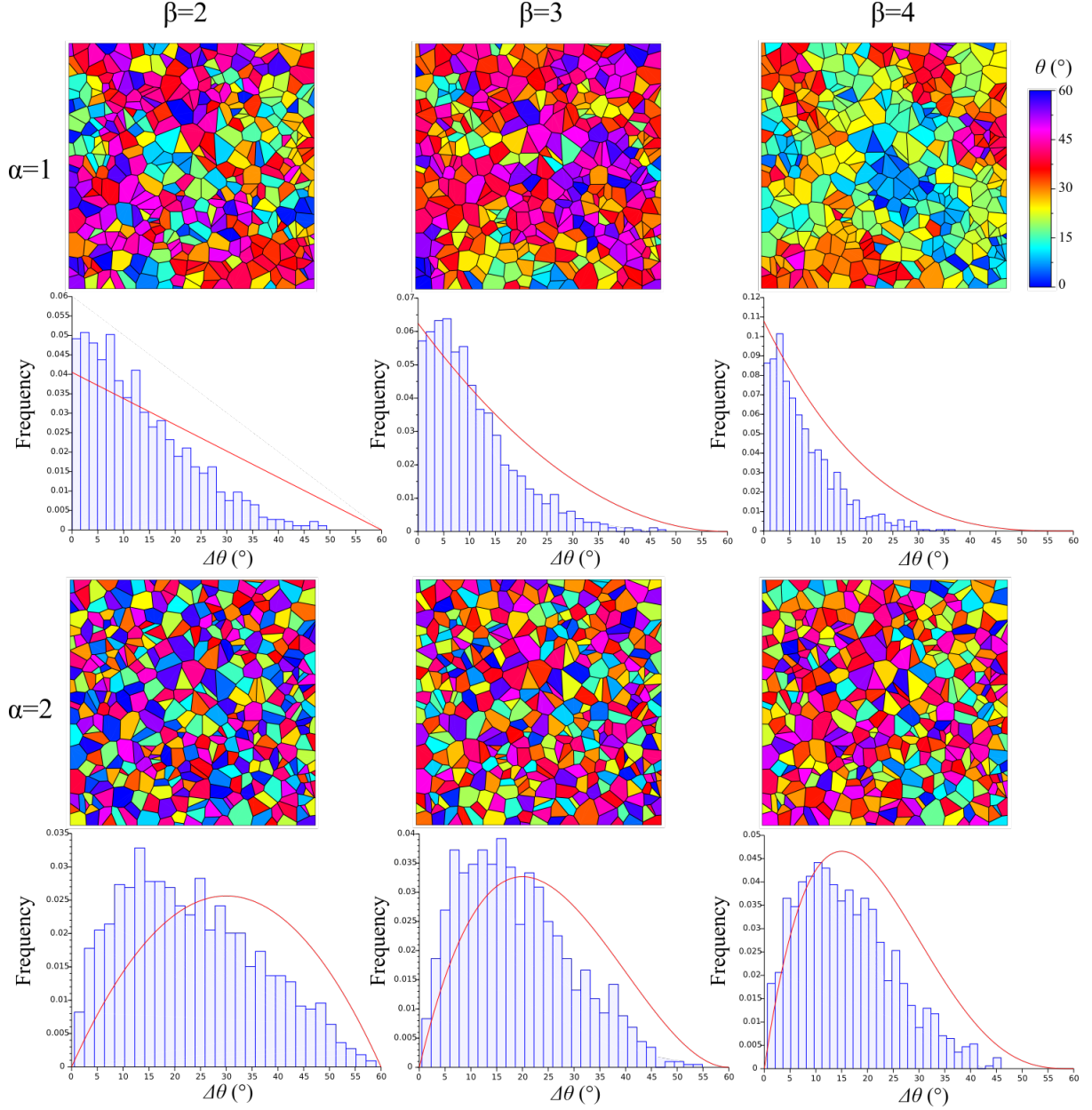


Figure 5: Examples of probabilistic orientation assignment. OTs with BMD histograms and targeted probability density function (red line)

the other grains are fixed. Therefore, the set of parameters describing the RVE is denoted by \mathcal{P}_{RVE} and reads:

$$\mathcal{P}_{\text{RVE}} = \left\{ \alpha = (\mathbf{x}, \mathbf{y}, \mathbf{w}, \boldsymbol{\theta}) \in [0, 1]^n \times [0, 1]^n \times \mathbb{R}^n \times \left[0, \frac{\pi}{3}\right]^n \right\} \quad (12)$$

It should be mentioned that the constraint (3) that applies to the entire OT, does not apply to the RVE. Indeed, the constraint implies that there are $N - 1$ independent weights. The n weights of the RVE are therefore independent. The set \mathcal{P}_{RVE} is a $4n$ dimensional vector space. The evolution law for the RVE is similar to (8) and reads for $\alpha = (\mathbf{x}, \mathbf{y}, \mathbf{w}, \boldsymbol{\theta}) \in \mathcal{P}_{\text{RVE}}$: $\dot{\mathbf{w}} = f(\alpha)$.

As the weights of grains surrounding the RVE are fixed, if the evolution law is not constrained, then the RVE tends to shrink to minimize the GB energy similarly to a spherical grain

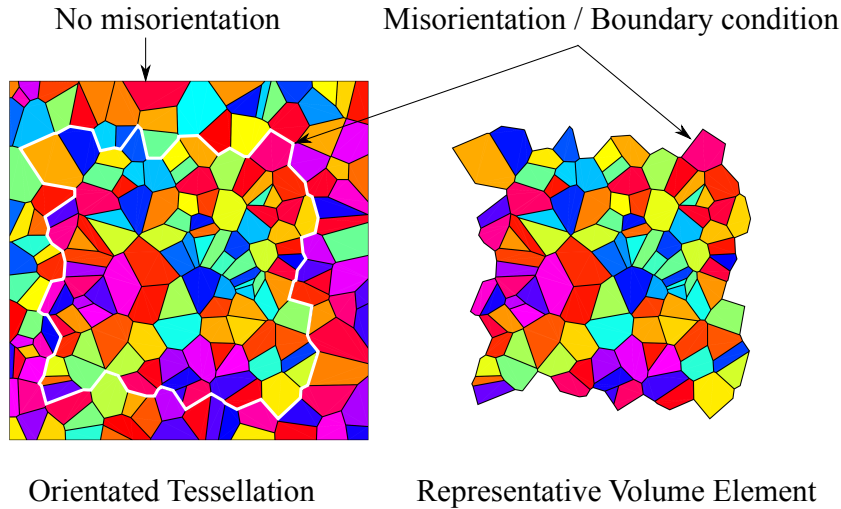


Figure 6: Definition of the RVE with boundary condition

in an infinite matrix. This issue is overcome by imposing mass conservation for the RVE as a constraint. This anomalous shrinkage is demonstrated as follows. A RVE is defined from an OT. A reference computation is performed for the entire OT (all weights are updated at each time step). In this case there is no constraint, as mass conservation is automatically verified. Then, two computations (with and without mass conservation) are performed for the RVE, and compared to the reference computation. The evolution law is derived in section 6, the purpose in this section being only to present the effect of mass conservation of the RVE. Results are presented in figure 7 (to facilitate the interpretation, grains not belonging to the RVE are distinguished by a white solid line). The OT physical size is $L_0 = 1$ mm, and initially consists of 200 grains. The figure 7 clearly shows that ensuring mass conservation in the mesoscopic evolution law enables to overcome the difficulty, even though it does not enable to obtain exactly the same evolution as the entire OT.

4.2. Mass conservation

Mass conservation has been introduced as an ad hoc principle in order to avoid anomalous shrinkage of RVEs. Mass is automatically conserved in OTs as they represent the entire object (no surrounding grains). However, the RVE exchanges matter with the rest of the OT (some grains grow at the expense of grains not belonging to the RVE) and mass conservation is not guaranteed. Ultimately, if the RVE were constituted of a single grain, then mass conservation principle would be obviously violated. Nevertheless, if a sufficient number of grains are considered in the RVE, the growth of some grains compensates the shrinkage of the others, and mass is statistically conserved (even though there are slight variations). This idea is demonstrated as follows. The evolution of an OT containing initially 5000 grains is computed (see figure 8). This OT represents a square sample with a side $L_0 \approx 7$ mm. The average grain size is around $100 \mu\text{m}$. The total mass is conserved as the OT does not exchange mass with the exterior. In contrast, several groups of connected grains are randomly selected in the OT and their mass is computed as a function of time. (In practice the surface is computed as the density is constant). For instance, the evolution of 9 groups is presented in figure 9. The positive relative

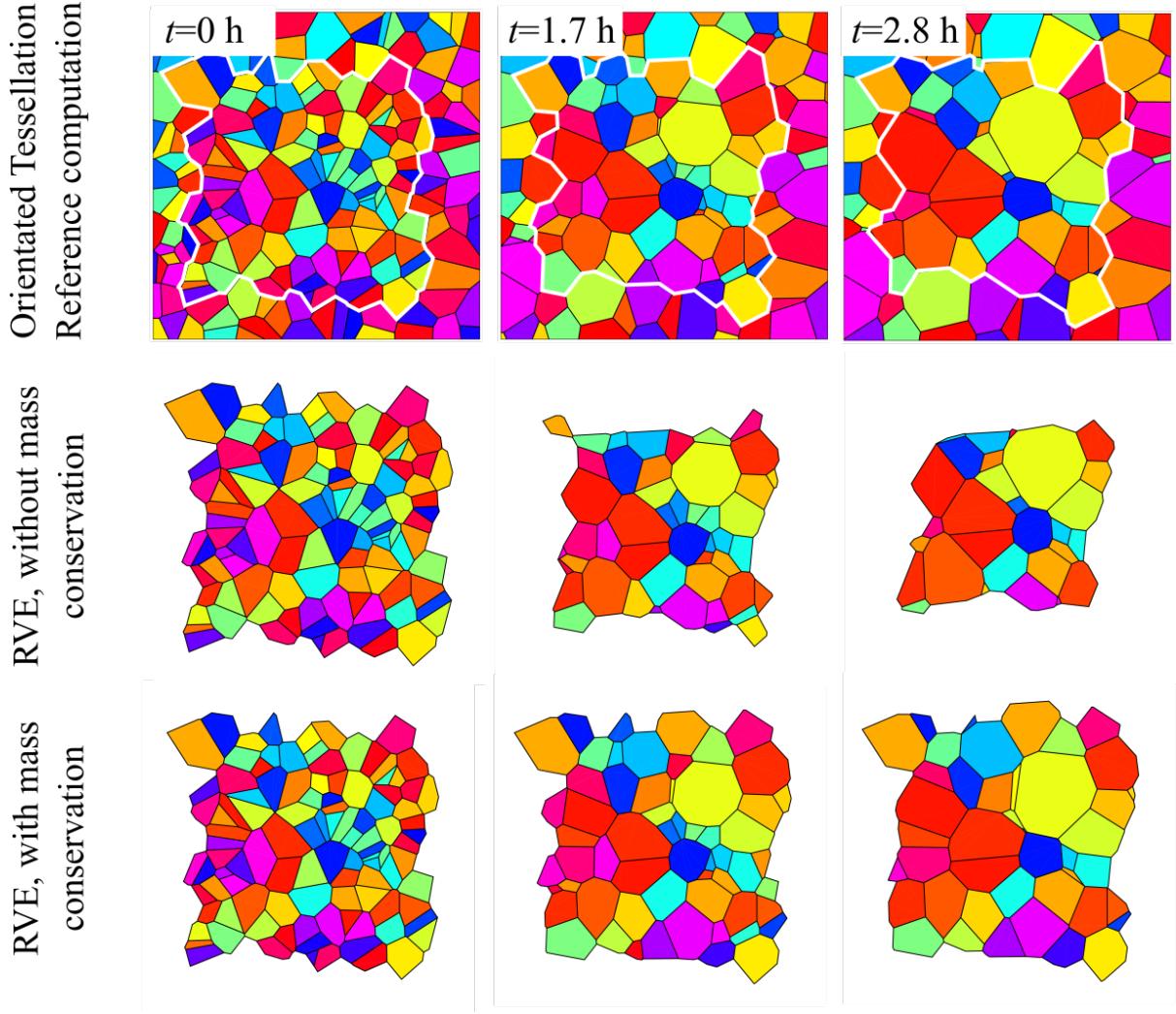


Figure 7: Comparison between OT and RVE respective evolutions (with or without mass conservation)

mass variation is denoted by $\Delta\varepsilon(t)$ and reads:

$$\Delta\varepsilon(t) = \frac{|M_{\text{RVE}}(t) - M_{\text{RVE}}(0)|}{M_{\text{RVE}}(0)} \quad (13)$$

where $M_{\text{RVE}}(t)$ is the mass of the group at time t . For each group, $t_{\text{RVE}}^{x\%}$ denotes the time needed to decrease the initial number of grains n_{RVE} by $x\%$. The maximum relative mass variation until $t_{\text{RVE}}^{x\%}$ is denoted by $\Delta\varepsilon_m^{x\%}$ and reads:

$$\Delta\varepsilon_m^{x\%} = \max_{t \in [0, t_{\text{RVE}}^{x\%}]} \Delta\varepsilon(t) \quad (14)$$

For each group, the maximum relative mass variation until the initial number of grains decreases by 33% is presented in figure 10. For groups with more than 110 grains $\Delta\varepsilon_m^{33\%}$ is below 4%. Thus, even for significant evolution, mass conservation is approximately verified for sufficiently large groups of connected grains. For smaller groups $\Delta\varepsilon_m^{33\%}$ may reach higher values, and the statistical mass conservation is not guaranteed. This analysis enables to determine the minimal number of grains to obtain an approximate statistical mass conservation.

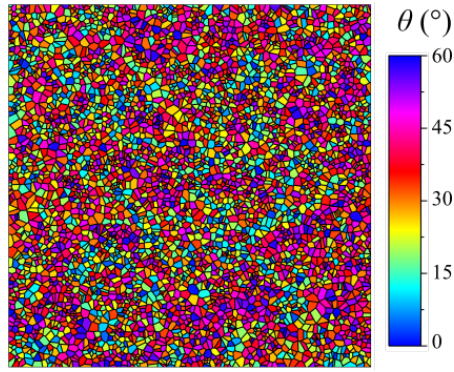


Figure 8: Initial 5000 grains polycrystal

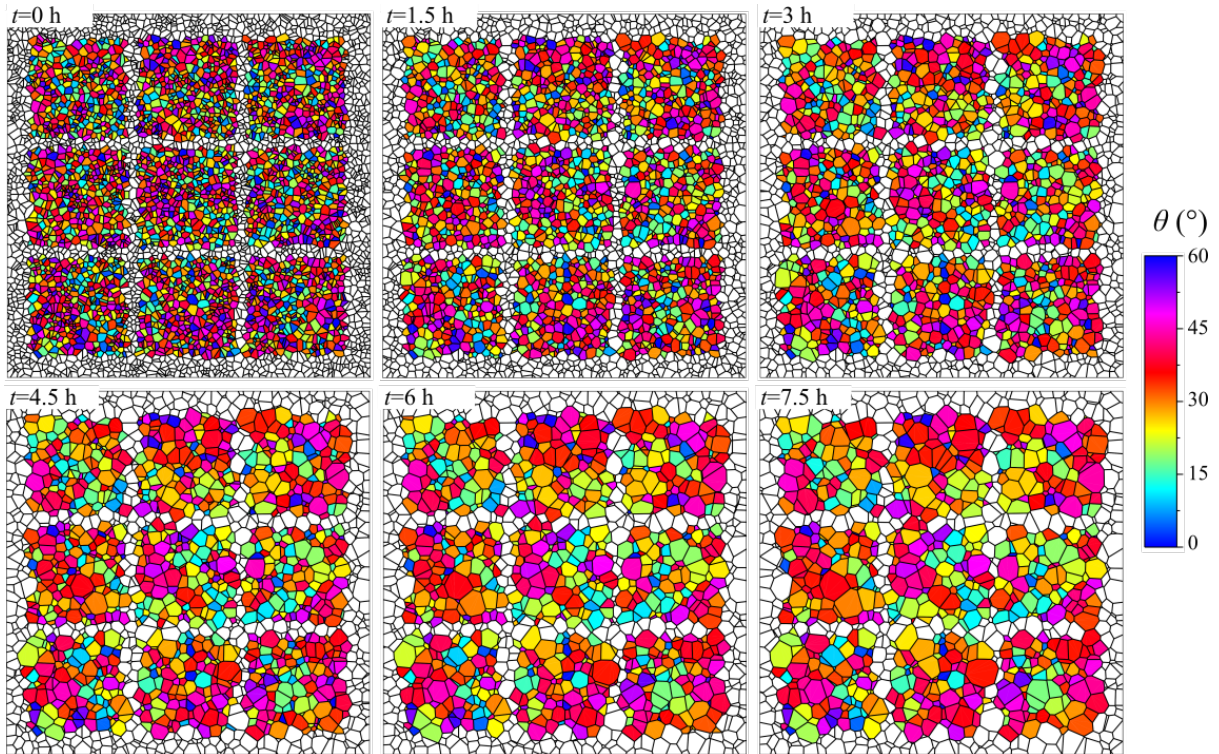


Figure 9: Evolution of 9 groups of connected grains in a 5000 grains polycrystal

5. Microscale mechanisms

Before establishing the mesoscopic evolution law taking into account mass conservation (see section 6), energetic mechanisms at the microscopic scale are introduced so that the mesoscopic evolution law relies on a physically consistent basis. Indeed, different energetic contributions are considered at the microscopic scale, namely: (i) the anisotropic GB energy (due to crystallographic misorientation) and (ii) the dissipated power due to crystal plasticity for very low angle boundaries and atomic jumps and atomic diffusion for high and intermediate angle boundaries respectively.

5.1. Grain boundary energy

GBs are defects that have an excess free energy per unit area with respect to the default stack energy. Indeed, the GB thickness is of a few atomic planes, where crystal lattices are disturbed

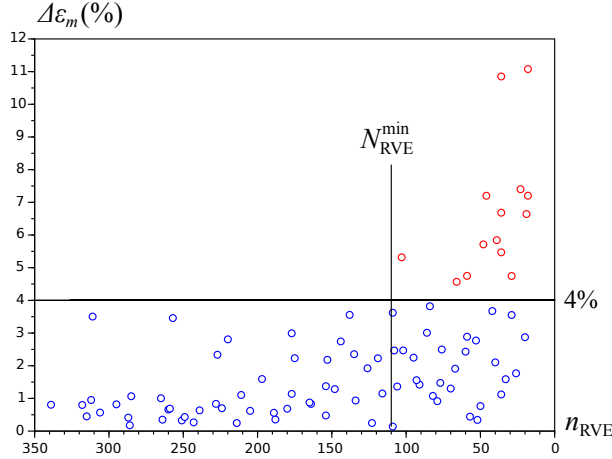


Figure 10: Determination of the minimum size of the RVE

to accommodate geometrical incompatibilities due to misorientation. In addition to temperature, five independent parameters enables to classify GBs (three describe the misorientation and two describe the orientation of the GB plane). In 2D, only two independent parameters are necessary (one describes the misorientation and one the GB plane). Various methods have been developed to compute and measure GB energy as a function of these five parameters (see [40] for a review of the literature). Thus, considering two-dimensional setting, the energy per unit area γ_{ij} of the GB between grains i and j (i.e., $(i, j) \in I_{\text{RVE}}$) reads:

$$\gamma_{ij} = \gamma(T, \Delta\theta_{ij}, \varphi_{ij}) \quad (15)$$

where γ is a function to be determined, T is the temperature, $\Delta\theta_{ij}$ is the crystal lattice misorientation between grains i and j defined by:

$$\Delta\theta_{ij} = |\theta_j - \theta_i| \in \left[0, \frac{\pi}{3}\right] \quad (16)$$

and where φ_{ij} is the angle of the GB plane. In 2D, one of the most popular approach is the Read & Shockley [41] model relying on dislocation calculation within the framework of continuum mechanics. An explicit analytic GB energy as a function of misorientation and GB plane orientation has been obtained. However, the range of validity of the Read & Shockley formula is limited to small misorientation angles and do not account for the energy cusps at certain misorientation angles. To overcome this difficulty, molecular dynamic computations have been proposed to compute GB energies as a function of the five parameters characterizing GBs. Among early works, Wolf [42–45] provided a systematic investigation of GB energy in fcc metals. Many other molecular dynamic computations have been carried out to determine GB energy (e.g., [46–48]). However, using molecular dynamics online during a simulation of grain growth would be computationally costly. Thus, some approaches attempt to establish simple models of GB energy based on multiscale strategies relying on molecular dynamic computations (e.g., [49]), whereas other approaches simply rely on interpolations of molecular dynamic computations (e.g., [50]). In this contribution such a strategy is adopted, molecular dynamic computations are performed and then interpolated as a function of misorientation.

To reduce the number of computations, it is assumed that the dependence on φ is negligible. Thus, the function $\gamma(T, \Delta\theta, \varphi)$ is approximated by a function $\gamma(T, \Delta\theta)$. Thus, $\langle 111 \rangle$ symmetric

tilt boundaries have been simulated for various misorientation angles $\Delta\theta$. GB energies were computed by minimizing system energy using the conjugate-gradient method in the LAMMPS code [51] at $T = 0$ K with embedded-atom method (EAM) interatomic potentials. The chosen interatomic potential [52] is adapted for Fe (pure iron) and presents the advantage to be stable at low temperature for fcc (although Fe presents a bcc structure at low temperature). The interatomic distance for the fcc structure is $a \approx 3.6057 \text{ \AA}$, and the default stack energy is $E_{ds} \approx 4.18127 \text{ eV}$ (exact values can be found on the OpenKIM project <https://openkim.org> [53]). The approach is similar to [46, 47], using computation cell with periodic boundary conditions. The misorientation angle is defined by two integers n_x and n_y , as shown in figure 11. For instance, for $\langle 001 \rangle$ tilt in fcc structures, periodicity leads to consider square simulation cell with a side being a multiple of $a\sqrt{n_x^2 + n_y^2}$ (see figure 11 left). However, for $\langle 111 \rangle$ tilt in fcc structures, periodicity leads to consider prismatic simulation cell with a $\pi/3$ skew angle as shown in figure 11 right, and a side being a multiple of $(a/\sqrt{2})\sqrt{n_x^2 + n_y^2 + n_x n_y}$.

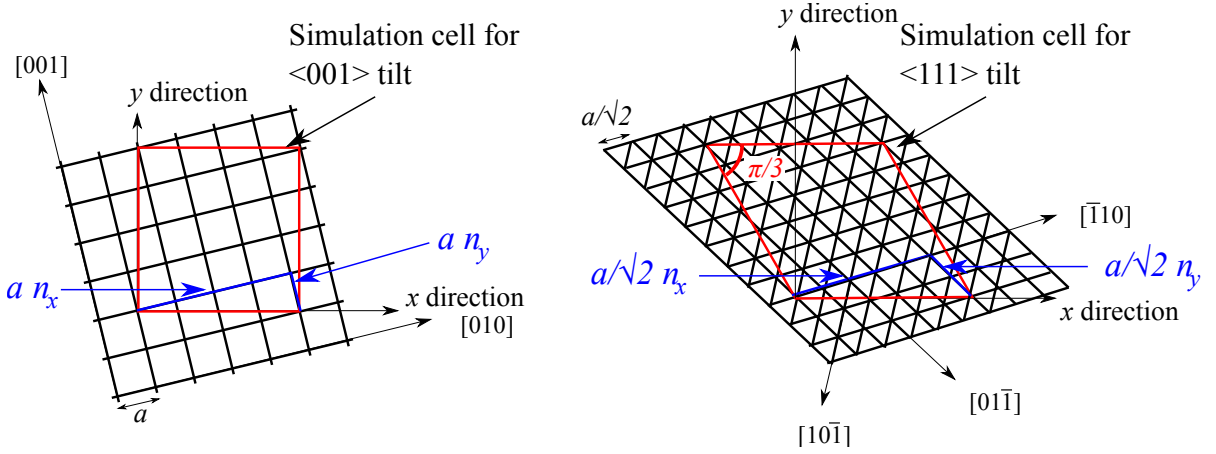


Figure 11: Simulation cell for molecular dynamic computations

Similarly to [47], a rigid body translation of one lattice with respect to the other is used to sample different starting configurations. In addition, since atoms in the two lattices are built up to the GB plane, an atom deletion criterion is used to remove atoms that may physically lie too close to each other. For each misorientation angle $\Delta\theta$, different rigid body translations ($0a$ to $0.5a$ with a step of $0.05a$) and atom deletion criteria ($0.3a$ to $0.7a$ with a step of $0.05a$), are tested, and only the minimum GB energy is stored for each tested misorientation angle. Results are presented in figure 12 with a piecewise interpolation function introduced in [54]:

$$\begin{cases} \gamma(0, \Delta\theta) = \gamma_1 \sin\left(\frac{\pi}{2} \frac{\Delta\theta}{\Delta\theta_1}\right) \left[1 - a_1 \ln\left(\sin\left(\frac{\pi}{2} \frac{\Delta\theta}{\Delta\theta_1}\right)\right)\right] \\ (0 \leq \Delta\theta \leq \Delta\theta_1) \\ \gamma(0, \Delta\theta) = \gamma_2 + (\gamma_1 - \gamma_2) \sin\left(\frac{\pi}{2} \frac{\Delta\theta - \frac{\pi}{3}}{\Delta\theta_1 - \frac{\pi}{3}}\right) \left[1 - a_2 \ln\left(\sin\left(\frac{\pi}{2} \frac{\Delta\theta - \frac{\pi}{3}}{\Delta\theta_1 - \frac{\pi}{3}}\right)\right)\right] \\ \left(\Delta\theta_1 \leq \Delta\theta \leq \frac{\pi}{3}\right) \end{cases} \quad (17)$$

where $\gamma_1 = 0.95 \text{ J.m}^{-2}$, $\gamma_2 = 0.67 \text{ J.m}^{-2}$, $a_1 = 0.5$, $a_2 = 0.1$ and $\Delta\theta_1 = \pi/6$.

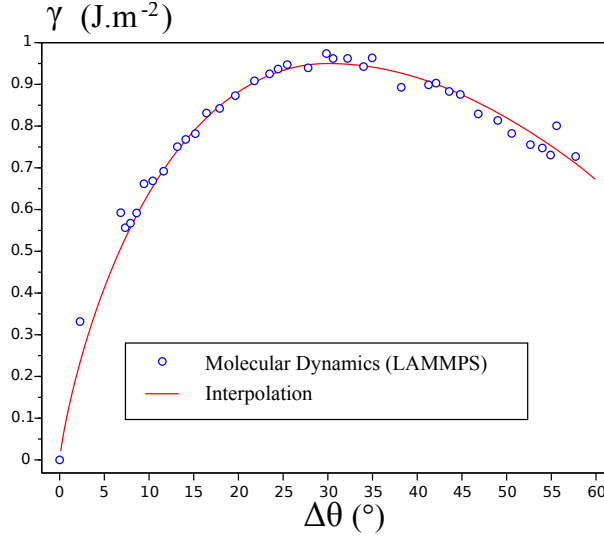


Figure 12: Grain boundary energy per unit area at $T = 0$ K for symmetric tilt $\langle 111 \rangle$

The grain GB energy has been interpolated for $T = 0$ K (i.e., $\gamma(0, \Delta\theta)$). However, the temperature dependence of GB energy is needed for simulating grain growth. In this contribution, we assume that the temperature dependence is in $G(T)/G(0)$ similarly to [55], where $G(T)$ is the shear coefficient:

$$\gamma(T, \Delta\theta) = \frac{G(T)}{G(0)} \gamma(0, \Delta\theta) \quad (18)$$

Data for Fe extracted from [56] are used to calibrate $G(T)$:

$$G(T) = a_G T + b_G \quad (19)$$

where $b_G \approx 88134$ MPa and $a_G \approx -24$ MPa.K⁻¹.

5.2. Dissipated power through grain boundary motion

Grain boundary energy enables to compute the driving force that tends to make evolve the system. Moreover, resistive mechanisms should be considered to control the speed at which the system may evolve. Thus, the dissipated power through any virtual motion of the GB is detailed in this section. For very low angle boundaries, the dissipative mechanism during GB motion can be interpreted within the framework of crystal plasticity. Indeed, slip systems are activated so that the crystal orientation of one grain can be transformed into the crystal orientation of the other grain, as shown in figure 13a (where v^* is a virtual normal velocity of the GB).

Consider v_{ij}^* a virtual velocity of the grain boundary (i, j). The dissipated power per unit area reads:

$$D_{ij}^* = D(T, \Delta\theta_{ij}, v_{ij}^*) \quad (20)$$

where D is a function to be determined. In [57, 58], D has been determined analytically within the framework of crystal plasticity. The calculation relies on two plane hexagonal semi-infinite crystals with a moving GB. Thus, six slip systems may be activated to transform the crystal orientation in the volume covered by the GB during motion (see. figure 13a). For practical calculation, the plastic slip is assumed to obey Schmid's law without hardening, while elasticity is neglected. The following dissipated power per unit area is obtained:

$$D(T, \Delta\theta_{ij}, v_{ij}^*) = \tau_c X(\Delta\theta_{ij}) |v_{ij}^*| \quad (21)$$

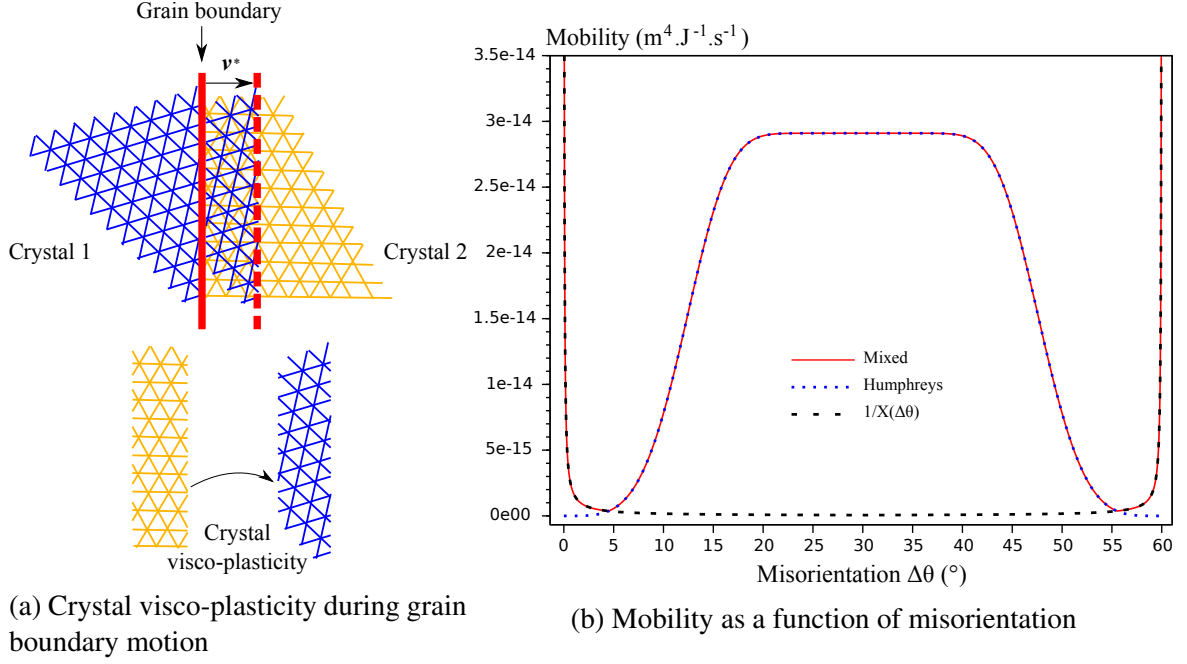


Figure 13: Dissipative mechanisms and mobility

where τ_c is the critical shear stress and X is the following function:

$$X(\Delta\theta) = \frac{6}{\pi} \left(\frac{\pi}{3} + 2\sqrt{3} \ln \left(\frac{\sqrt{3}}{2} \right) \right) \min \left\{ \Delta\theta, \frac{\pi}{3} - \Delta\theta \right\} \quad (22)$$

Since grain growth is viscous, the analytic computation proposed in [57, 58] is simply adapted for crystal visco-plasticity by considering that the critical shear stress τ_c linearly depends on $|v_{ij}^*|$, which reads:

$$\tau_c = \frac{1}{m(T)} |v_{ij}^*| \quad (23)$$

where $m(T)$ is a grain mobility ($\text{m}^4.\text{J}^{-1}.\text{s}^{-1}$) that can be related to the curvature driven mobility $m_{CD}(T, \Delta\theta)$ introduced in (1). The mobility $m(T)$ is calibrated so that the shrinkage of an hexagonal grain (computed according to the present model) evolves at the same speed as the shrinkage of a circular grain according to the curvature driven evolution law (1). More precisely, it is shown in Appendix B that:

$$m_{CD}(T, \Delta\theta) = \frac{m(T)}{X(\Delta\theta)} \quad (24)$$

Hence the dissipated power per unit area:

$$D(T, \Delta\theta_{ij}, v_{ij}^*) = \frac{[v_{ij}^*]^2}{m_{CD}(T, \Delta\theta)} \quad (25)$$

Thus, the dissipated power (25) corresponds to what is obtained for the curvature driven growth.

For very low angle boundaries, $m_{CD}(T, \Delta\theta)$ varies in $1/\Delta\theta$ (see (24)), which is consistent with the expression obtained by considering the movement of boundaries in which the dislocations are spaced far apart [1]. However, for high angle boundaries the dislocation cores overlap,

and the dissipative mechanism is more likely related to atom jumps, and for intermediate angle boundaries, dissipation is attributed to diffusion of atoms over a certain distance [1]. Since the mobility completely determines the dissipated power through any virtual speed (see (25)), real dissipative mechanisms are indirectly taken into account in the mobility function $m_{CD}(T, \Delta\theta)$. There are significant evidences [1] that for intermediate and high angle boundaries the mobility can be approximated by the following sigmoid function introduced in [59, 60]:

$$m_{CD}(T, \Delta\theta) = m_{\max}(T) \left(1 - \exp \left[-K \left(\frac{\Delta\theta}{\Delta\theta_1} \right)^p \right] \right) \quad (26)$$

where K is a positive coefficient, p is positive exponent, m_{\max} is the maximum mobility and $\Delta\theta_1$ is a threshold. However, (26) should not be used for very low angle boundaries because $m_{CD}(T, \Delta\theta)$ would tend to 0 when $\Delta\theta$ tends to zero which would lead to an infinite dissipated power (see (25)). This difficulty is overcome in this paper by introducing a mixed mobility based on (24) for very low angle boundaries and (26) for higher angle boundaries, which reads:

$$m_{CD}(T, \Delta\theta) = \begin{cases} \frac{m(T)}{X(\Delta\theta)} & \text{if } \min \left\{ \Delta\theta, \frac{\pi}{3} - \Delta\theta \right\} \leq \Delta\theta_0 \\ m_{\max}(T) \left(1 - \exp \left[-K \left(\frac{\Delta\theta}{\Delta\theta_1} \right)^p \right] \right) & \text{if } \min \left\{ \Delta\theta, \frac{\pi}{3} - \Delta\theta \right\} \geq \Delta\theta_0 \end{cases} \quad (27)$$

where $\Delta\theta_0$ is a threshold between very low angle boundaries and high and intermediate angle boundaries. In addition, continuity reads:

$$m(T) = m_{\max}(T) \left(1 - \exp \left[-K \left(\frac{\Delta\theta_0}{\Delta\theta_1} \right)^p \right] \right) X(\Delta\theta_0) \quad (28)$$

In figure 13b the mobility (27) is presented with parameters listed in table 1.

6. Mesoscopic evolution law

In this section, the mesoscopic evolution law accounting for mass conservation is derived. This evolution law is adapted for RVEs with boundary conditions (see section 4.1). The total energy per unit depth (denoted by \mathcal{E}) is considered in the RVE as well as the total dissipated power per unit depth (denoted by \mathcal{D}). For $\alpha \in \mathcal{P}_{\text{RVE}}$:

$$\begin{cases} \mathcal{E}(T, \alpha) = L_0 \sum_{(i,j) \in I_{\text{RVE}}} l_{ij} \gamma_{ij} \\ \mathcal{D}(T, \alpha, \mathbf{v}^*) = L_0 \sum_{(i,j) \in I_{\text{RVE}}} l_{ij} D_{ij}^* \end{cases} \quad (29)$$

where $I_{\text{RVE}} \subset I_{\text{GB}}$ is the set of GBs in the RVE. There are n grains in the RVE and n_{GB} GBs with $n_{\text{GB}} = \text{card}[I_{\text{RVE}}]$. In addition, l_{ij} is the dimensionless joint length, and γ_{ij} and D_{ij}^* are computed from (18) and (25) respectively. Moreover, \mathbf{v}^* is the following vector:

$$\mathbf{v}^* = \left(v_{ij}^* \right)_{(i,j) \in I_{\text{RVE}}} \quad (30)$$

By combining (25) and (30) one obtains:

$$\mathcal{D}(T, \alpha, \mathbf{v}^*) = L_0 \mathbf{v}^* \cdot \chi(T, \alpha) \cdot \mathbf{v}^* \quad (31)$$

where $\chi(\alpha)$ is a diagonal second order tensor of size $n_{GB} \times n_{GB}$ whose diagonal reads:

$$\forall (i, j) \in I_{RVE}, \quad \chi(T, \Delta\theta_{ij}) = \frac{l_{ij}}{m_{CD}(T, \Delta\theta_{ij})} \quad (32)$$

As seeds and crystalline orientations are fixed (i.e., $\dot{\mathbf{x}} = \dot{\mathbf{y}} = 0$ and $\dot{\boldsymbol{\theta}} = 0$), and considering any virtual variation of weights $\dot{\mathbf{w}}^*$, it is straightforward to demonstrate that:

$$v_{ij}^* = L_0 \frac{\dot{w}_i^* - \dot{w}_j^*}{2d_{ij}} \quad (33)$$

where d_{ij} is the dimensionless distance between seeds:

$$d_{ij} = \left\| \begin{pmatrix} x_i \\ y_i \end{pmatrix} - \begin{pmatrix} x_j \\ y_j \end{pmatrix} \right\| \quad (34)$$

It is clear in (33) that for each GB an arbitrary choice is made for the positive direction of the normal velocity v_{ij}^* , which has no consequence as the square of the virtual velocity arises in the dissipated power. Hence:

$$\mathbf{v}^* = L_0 \mathbf{K}(\alpha) \cdot \dot{\mathbf{w}}^* \quad (35)$$

where $\mathbf{K}(\alpha)$ is a second order tensor of size $n_{GB} \times n$, which can be evaluated analytically:

$$\mathbf{K}(\alpha) = {}_{(i,j)} \begin{matrix} & & & i & & & & j & & & & \\ \begin{bmatrix} \vdots & \vdots \\ 0 & \cdots & 0 & \frac{1}{2d_{ij}} & 0 & \cdots & 0 & -\frac{1}{2d_{ij}} & 0 & \cdots & 0 \\ \vdots & \vdots \end{bmatrix} & & & & & & & & & & & \end{matrix} \quad (36)$$

The tensor $\mathbf{K}(\alpha)$ represents the link between the normal speed of the n_{GB} GBs and the n weights. However, only the weights are controlled in the evolution law. Thus, consider $\mathbf{R}(\alpha)$ the following second order tensor of size $n \times n$:

$$\mathbf{R}(T, \alpha) = \mathbf{K}(\alpha)^T \cdot \chi(T, \alpha) \cdot \mathbf{K}(\alpha) \quad (37)$$

As already mentioned, the constraint (3) does not apply for the RVE (only for the entire OT), thus $\mathbf{R}(T, \alpha)$ is invertible and symmetrical positive-definite. For any virtual weight variation $\dot{\mathbf{w}}^*$, the total dissipated power per unit depth reads:

$$\mathcal{D}(T, \alpha, \dot{\mathbf{w}}^*) = L_0^3 \dot{\mathbf{w}}^* \cdot \mathbf{R}(T, \alpha) \cdot \dot{\mathbf{w}}^* \quad (38)$$

The energy balance equation obtained from the first and second laws of thermodynamics holds for any possible state α and any possible evolution $\dot{\mathbf{w}}$ (real not virtual):

$$\mathcal{D}(T, \alpha, \dot{\mathbf{w}}) + \dot{\mathcal{E}}(T, \alpha) = 0 \quad (39)$$

Hence:

$$L_0^3 \dot{\mathbf{w}} \cdot \mathbf{R}(T, \alpha) \cdot \dot{\mathbf{w}} + \frac{\partial \mathcal{E}}{\partial \mathbf{w}}(T, \alpha) \cdot \dot{\mathbf{w}} = 0 \quad (40)$$

In addition, the mass balance equation reads (if density is assumed constant):

$$\dot{S}(\alpha) = \frac{\partial S}{\partial \mathbf{w}} \cdot \dot{\mathbf{w}} = 0 \quad (41)$$

where S denotes the total area of the n grains in the RVE.

The maximum dissipation principle [61] under the constraint (40) and (41) is invoked to determine the evolution law:

$$\dot{\mathbf{w}}_{\text{meso}} = \begin{cases} \operatorname{argmax}_{\dot{\mathbf{w}} \in \mathbb{R}^n} \left[L_0^3 \dot{\mathbf{w}} \cdot \mathbf{R}(T, \alpha) \cdot \dot{\mathbf{w}} \right] \\ \text{subjected to. } L_0^3 \dot{\mathbf{w}} \cdot \mathbf{R}(T, \alpha) \cdot \dot{\mathbf{w}} + \frac{\partial \mathcal{E}}{\partial \mathbf{w}}(T, \alpha) \cdot \dot{\mathbf{w}} = 0 \\ \frac{\partial S}{\partial \mathbf{w}} \cdot \dot{\mathbf{w}} = 0 \end{cases} \quad (42)$$

The maximization problem (42) is solved analytically by Lagrangian multiplier method. Consider the following Lagrangian:

$$\mathcal{L}(\dot{\mathbf{w}}, \lambda_1, \lambda_2) = L_0^3 \dot{\mathbf{w}} \cdot \mathbf{R} \cdot \dot{\mathbf{w}} + \lambda_1 \left(L_0^3 \dot{\mathbf{w}} \cdot \mathbf{R} \cdot \dot{\mathbf{w}} + \frac{\partial \mathcal{E}}{\partial \mathbf{w}} \cdot \dot{\mathbf{w}} \right) + \lambda_2 \frac{\partial S}{\partial \mathbf{w}} \cdot \dot{\mathbf{w}} \quad (43)$$

The optimality condition reads:

$$\frac{\partial \mathcal{L}}{\partial \dot{\mathbf{w}}} = 2L_0^3 (1 + \lambda_1) \mathbf{R} \cdot \dot{\mathbf{w}} + \lambda_1 \frac{\partial \mathcal{E}}{\partial \mathbf{w}} + \lambda_2 \frac{\partial S}{\partial \mathbf{w}} = 0 \quad (44a)$$

$$\frac{\partial \mathcal{L}}{\partial \lambda_1} = L_0^3 \dot{\mathbf{w}} \cdot \mathbf{R} \cdot \dot{\mathbf{w}} + \frac{\partial \mathcal{E}}{\partial \mathbf{w}} \cdot \dot{\mathbf{w}} = 0 \quad (44b)$$

$$\frac{\partial \mathcal{L}}{\partial \lambda_2} = \dot{\mathbf{w}} \cdot \frac{\partial S}{\partial \mathbf{w}} = 0 \quad (44c)$$

Contracting (44a) with $\dot{\mathbf{w}}$, one obtains:

$$2L_0^3 (1 + \lambda_1) \dot{\mathbf{w}} \cdot \mathbf{R} \cdot \dot{\mathbf{w}} + \lambda_1 \frac{\partial \mathcal{E}}{\partial \mathbf{w}} \cdot \dot{\mathbf{w}} + \lambda_2 \dot{\mathbf{w}} \cdot \frac{\partial S}{\partial \mathbf{w}} = 0 \quad (45)$$

Considering (44b) and (44c), (45) reduces to:

$$(2 + \lambda_1) \dot{\mathbf{w}} \cdot \mathbf{R} \cdot \dot{\mathbf{w}} = 0 \quad (46)$$

The tensor \mathbf{R} being symmetric definite-positive, $\dot{\mathbf{w}} \cdot \mathbf{R} \cdot \dot{\mathbf{w}} > 0$, thus:

$$\lambda_1 = -2 \quad (47)$$

Plugging (47) into (44a) one obtains:

$$\dot{\mathbf{w}}_{\text{meso}} = -\frac{1}{L_0^3} \left(\mathbf{R}^{-1} \cdot \frac{\partial \mathcal{E}}{\partial \mathbf{w}} - \frac{\lambda_2}{2} \mathbf{R}^{-1} \cdot \frac{\partial S}{\partial \mathbf{w}} \right) \quad (48)$$

The multiplier λ_2 is obtained by contracting (48) by $\partial S/\partial \mathbf{w}$ and using (44c):

$$\lambda_2 = 2 \frac{\frac{\partial S}{\partial \mathbf{w}} \cdot \mathbf{R}^{-1} \cdot \frac{\partial \mathcal{E}}{\partial \mathbf{w}}}{\frac{\partial S}{\partial \mathbf{w}} \cdot \mathbf{R}^{-1} \cdot \frac{\partial S}{\partial \mathbf{w}}} \quad (49)$$

By plugging (49) into (48) one obtains:

$$\dot{\mathbf{w}}_{\text{meso}} = -\frac{1}{L_0^3} \left[\mathbf{R}^{-1} \cdot \frac{\partial \mathcal{E}}{\partial \mathbf{w}} - \left(\frac{\frac{\partial S}{\partial \mathbf{w}} \cdot \mathbf{R}^{-1} \cdot \frac{\partial \mathcal{E}}{\partial \mathbf{w}}}{\frac{\partial S}{\partial \mathbf{w}} \cdot \mathbf{R}^{-1} \cdot \frac{\partial S}{\partial \mathbf{w}}} \right) \left(\mathbf{R}^{-1} \cdot \frac{\partial S}{\partial \mathbf{w}} \right) \right] \quad (50)$$

Thus, the mesoscopic evolution law reads:

$$\dot{\mathbf{w}}_{\text{meso}} = -\frac{\mathbf{M}(T, \boldsymbol{\alpha})}{L_0^3} \cdot \frac{\partial \mathcal{E}(T, \boldsymbol{\alpha})}{\partial \mathbf{w}} \quad (51)$$

where \mathbf{M} is a second order tensor of size $n \times n$ homogenous to a mobility ($\text{m}^4 \cdot \text{J}^{-1} \cdot \text{s}^{-1}$) defined as follows:

$$\mathbf{M} = \mathbf{R}^{-1} - \frac{\left(\mathbf{R}^{-1} \cdot \frac{\partial S}{\partial \mathbf{w}} \right) \otimes \left(\mathbf{R}^{-1} \cdot \frac{\partial S}{\partial \mathbf{w}} \right)}{\left(\frac{\partial S}{\partial \mathbf{w}} \cdot \mathbf{R}^{-1} \cdot \frac{\partial S}{\partial \mathbf{w}} \right)} \quad (52)$$

By using (29) and (18) the mesoscopic evolution law reads:

$$\dot{\mathbf{w}}_{\text{meso}} = -\frac{\mathbf{M}(T, \boldsymbol{\alpha})}{L_0^2} \cdot \left[\sum_{(i,j) \in I_{\text{RVE}}} \frac{\partial l_{ij}}{\partial \mathbf{w}} \gamma(T, \Delta \theta_{ij}) \right] \quad (53)$$

The viscous evolution law (53) presents a size effect through the scaling parameters L_0 . The tensor $\mathbf{M}(T, \boldsymbol{\alpha})$ is completely determined by the actual state $(\boldsymbol{\alpha}, T)$ of the RVE. The gradients $\partial l_{ij}/\partial \mathbf{w}$ and $\partial S/\partial \mathbf{w}$ are easily obtained by a geometrical analysis of the OT, which is detailed in [Appendix A](#).

For simulations of entire OTs in section 4 (i.e., all weights are updated and mass conservation is not imposed) the tensor \mathbf{M} in (53) should be replaced by:

$$\mathbf{M} = \mathbf{R}^\dagger \quad (54)$$

where \mathbf{R}^\dagger is the *Moore-Penrose* pseudo-inverse of \mathbf{R} that can be computed by singular value decomposition techniques. Indeed, because of the constraint (3), there are only $N - 1$ independent weights in the entire OT and \mathbf{R} is not invertible (rank $N - 1$). It is straightforward to show that the pseudo-inverse enables to obtain the $N - 1$ independent weights time derivatives.

7. Results

All Voronoi-Laguerre tessellations are produced by using the free software NEPER [29] and the evolution law (53) is computed by using the free software SCILAB [62]. The *dialogue* between NEPER and SCILAB is done by writing and reading text files (e.g., Voronoi-Laguerre tessellation files, list of updated weights etc.), which represents the most significant part of the computation time. Despite this unoptimal implementation, computation time is relatively short (e.g., a time increment for a 1000 grains OT is around 1 second on a personal computer). Computation time could be fairly reduced though by implementing the model in C++ language directly in NEPER.

7.1. Comparison with von Neumann-Mullins law

In this section, the mesoscopic model is compared to the von Neumann-Mullins (vNM) law [34, 35, 63]. The classical vNM law is formulated within a fully isotropic framework (i.e., isotropic GB energy and isotropic mobility), and relies on the curvature driving evolution law (1) and the assumption that angles at triple junctions are 120° . Thus, the vNM reads:

$$\frac{d}{dt}S_n = \frac{\pi m^*}{3}(n - 6) \quad (55)$$

where n is the number of sides of the grains family, dS_n/dt is the area change rate of n sided grains, and $m^* = \gamma m_{CD}$ ($\text{m}^2 \cdot \text{s}^{-1}$) is the constant reduced mobility. The vNM law (55) applies to individual n sided grains in 2D ideal grain growth [63]. In the following, we determine whether the vNM law is verified in average, where m^* is the average reduced mobility in the entire RVE. In addition, an extended vNM law (56) has also been proposed for anisotropic grain growth and tested with a mesoscopic stochastic Monte-Carlo simulations [35].

$$\frac{d}{dt}\langle S_n \rangle = \langle m_n^* \rangle (\pi - \langle \beta_n \rangle) \left(n - \frac{2\pi}{\pi - \langle \beta_n \rangle} \right) \quad (56)$$

where $\langle m_n^* \rangle$ is the average reduced mobility, $\langle \beta_n \rangle$ is the average triple junction angle, and where averages are taken over the family of the n sided grains. However, in Voronoi-Laguerre tessellations each grain is polygonal and then $\langle \beta_n \rangle = \pi(n - 2)/n$, and therefore $d\langle S_n \rangle/dt = 0$ in (56). Thus, the extended vNM law is of limited interest within the framework of OTUM. But a simple extended vNM law can be simply derived from (55) to take anisotropy into account:

$$\frac{d}{dt}\langle S_n \rangle = \frac{\pi \langle m_n^* \rangle}{3}(n - 6) \quad (57)$$

Three conditions are tested in the following and listed in table 1. A purely isotropic condition is tested with constant GB energy γ_0 and mobility m_0 listed in table 1. A weakly anisotropic condition is also considered with a constant reduced mobility $m^*(T)$ and an anisotropic GB energy $\gamma(T, \Delta\theta)$, hence $m_{CD}(T, \Delta\theta) = m^*(T)/\gamma(T, \Delta\theta)$, where $m^*(T)$ is given in table 1. Despite the anisotropic GB energy and mobility, this condition is similar to the isotropic condition with respect to the curvature driven relation (1), which only depends on the reduced mobility. A fully anisotropic condition is also tested by considering (27) whose parameters are listed in table 1.

A single 2500 grains tessellation is used, and the BMD is assigned as detailed in section 3 by a beta probability density function $\mathcal{B}(\alpha, \beta)$ with $\alpha = 2$, $\beta = 3$ (see figure 5). Numerical values

Table 1: Conditions related to GB energy, mobility and reduced mobility. For all conditions the average reduced mobility over the entire tessellation is $m^* = 0.06 \cdot 10^{-12} \text{ m}^2 \cdot \text{s}^{-1}$ and $T = 800^\circ$ (the symbol T is omitted).

	Isotropic 0	Anisotropic 1	Anisotropic 2 (27)
GB energy ($\text{J} \cdot \text{m}^{-2}$)	$\gamma_0 = 0.535$	$\gamma(\Delta\theta)$ (17)	$\gamma(\Delta\theta)$ (17)
Mobility ($\text{m}^4 \cdot \text{J}^{-1} \cdot \text{s}^{-1}$)	$m_0 = 1.112 \cdot 10^{-13}$	-	$m_{\max} = 0.291 \cdot 10^{-13}$
Reduced mobility ($\text{m}^2 \cdot \text{s}^{-1}$)	-	$m^* = 0.06 \cdot 10^{-12}$	-
Coefficient (-)	-	-	$K = 5$
Exponent (-)	-	-	$p = 4$
Misorientation angle (-)	-	-	$\Delta\theta_1 = \pi/9$
Misorientation angle (-)	-	-	$\Delta\theta_0 = 4.5\pi/180$

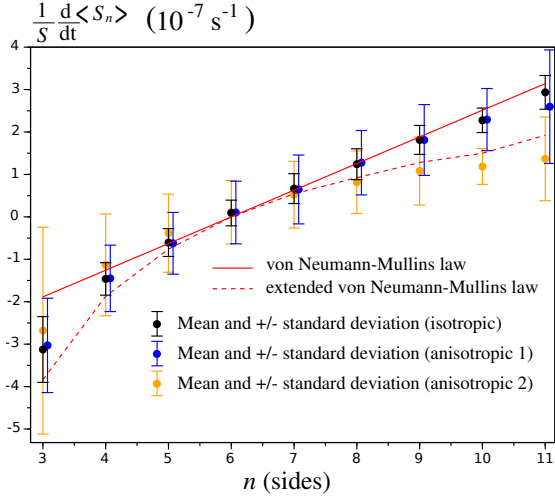
listed in table 1 have been chosen so that the average reduced mobility over the entire RVE is the same for all conditions. For each number of sides, the corresponding normalized area change rate distribution is computed. In figure 14a the mean values with standard deviations are presented as a function of the number of sides. As expected, the isotropic condition fits well with the vNM law with small standard deviations (excepted for grains with 3 sides). The same behavior is observed for condition 1 as the reduced mobility is also constant. Larger standard deviations are obtained though, as the vNM law (55) relies on isotropic energy, which is not verified for condition 1. Results for condition 2 fits better with the extended vNM law (57), which is due to the anisotropy. This result is similar to what is obtained in [35] for the same condition.

7.2. Comparison with Hillert and Rayleigh distributions

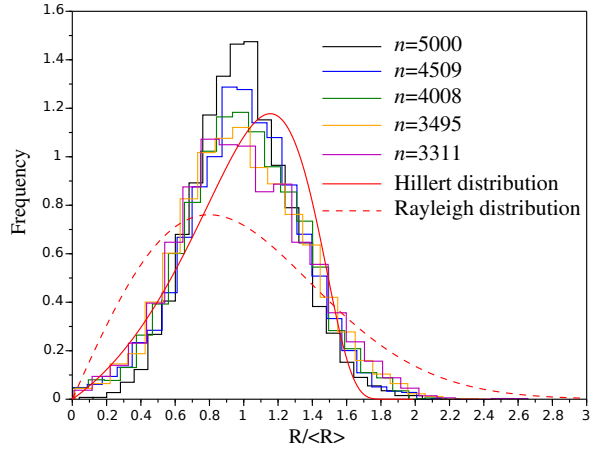
In this section, the equivalent grain size distribution $R/\langle R \rangle$ is analyzed (where R is the grain equivalent radius and $\langle R \rangle$ its average over the RVE). The well known Hillert [32] and Rayleigh distributions are compared to the model for all conditions listed in table 1. The tested OT has initially 5000 grains with a misorientation distribution defined by a beta probability density function $\mathcal{B}(\alpha, \beta)$ with $\alpha = 2, \beta = 3$. The histograms of $R/\langle R \rangle$ are given for different numbers of grains left in the tessellation after evolution. For all conditions, results are similar to what is observed for purely isotropic grain growth in [33]. Histograms for condition 2 are presented in figure 14b. The quasi steady-state distribution is in between Hillert and Rayleigh distributions, and can be fitted by a log-normal density function. In addition, the average grain size $\langle R \rangle$ is presented as a function of time in figure 15 for condition 2. The well-known grain growth power law $\langle R \rangle \sim t^n$ (where $n = 1/2$ as for isotropic grain growth) is rapidly reached by the proposed model.

7.3. Comparison with experiments

A recent experiment has been conducted on pure iron during annealing for 75 min at 800°C [36]. The sample is initially fully recrystallized. Grain evolution has been determined in three dimensions using diffraction contrast tomography at a synchrotron source. Since the present model has been derived in 2D, only a plane section of the sample is compared to the model at three different time steps (0 min, 40 min and 75 min). Approximating a real grain structure with a Voronoi-Laguerre tessellation is usually done by numerical optimization. However, as the proposed comparison is mostly qualitative, a rough approximation of the initial grain structure is proposed and crystal orientations have been assigned manually by following the

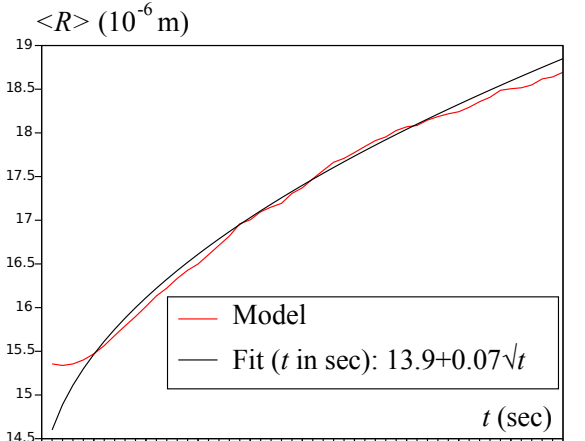


(a) Normalized average area change rate as a function of the number of sides, and comparison with (55) and (57). Error bars represent more or less one standard deviation. $d\langle S_n \rangle / dt$ is the average area change rate and S is the total area of the OT.

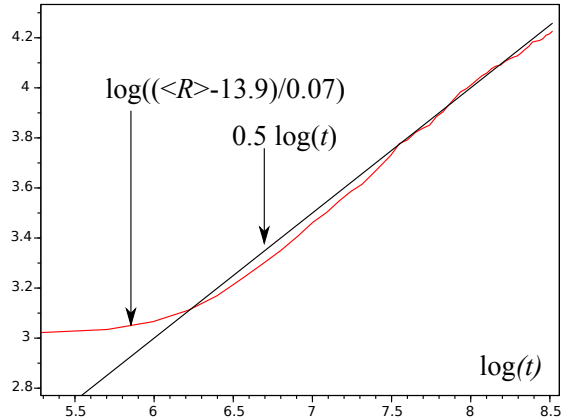


(b) Histograms of equivalent size distribution for different number of grains left in the polycrystal, and comparison with classical Hillert and Rayleigh distributions

Figure 14: Validation of basic grain statistics



(a) Average grain size $\langle R \rangle$ as a function of time



(b) Average grain size $\langle R \rangle$ as a function of time as a log-log plot

Figure 15: Validation of grain growth power law $\langle R \rangle \sim t^n$

misorientation estimation proposed in [36] (i.e., black and white lines represent boundaries with misorientations above and below 15° , respectively). The specimen in [36] is around $500 \mu\text{m}$ in diameter, and the best fit between the model and experimental results is obtained for $480 \mu\text{m}$. The reduced mobility has been estimated in [36], and linearly evolves during annealing from $0.12 \cdot 10^{-12} \text{ m}^2 \cdot \text{s}^{-1}$ to $0.02 \cdot 10^{-12} \text{ m}^2 \cdot \text{s}^{-1}$. The mobility (27) is considered with parameters are listed in table 1 excepted m_{max} that is set so that the average reduced mobility over the sample is $0.06 \cdot 10^{-12} \text{ m}^2 \cdot \text{s}^{-1}$. The GB energy is obtained by molecular dynamics computations on pure iron as shown in figure 12. The qualitative comparison is presented in figure 16 where grains are colored as in [36] to facilitate the reading. It should also be noted that several neighboring

grains have the same crystal orientations to form larger grains. The average equivalent grain radius $\langle R \rangle$ has been extracted from [36] and compared with the model. Good agreement is observed in figure 17.

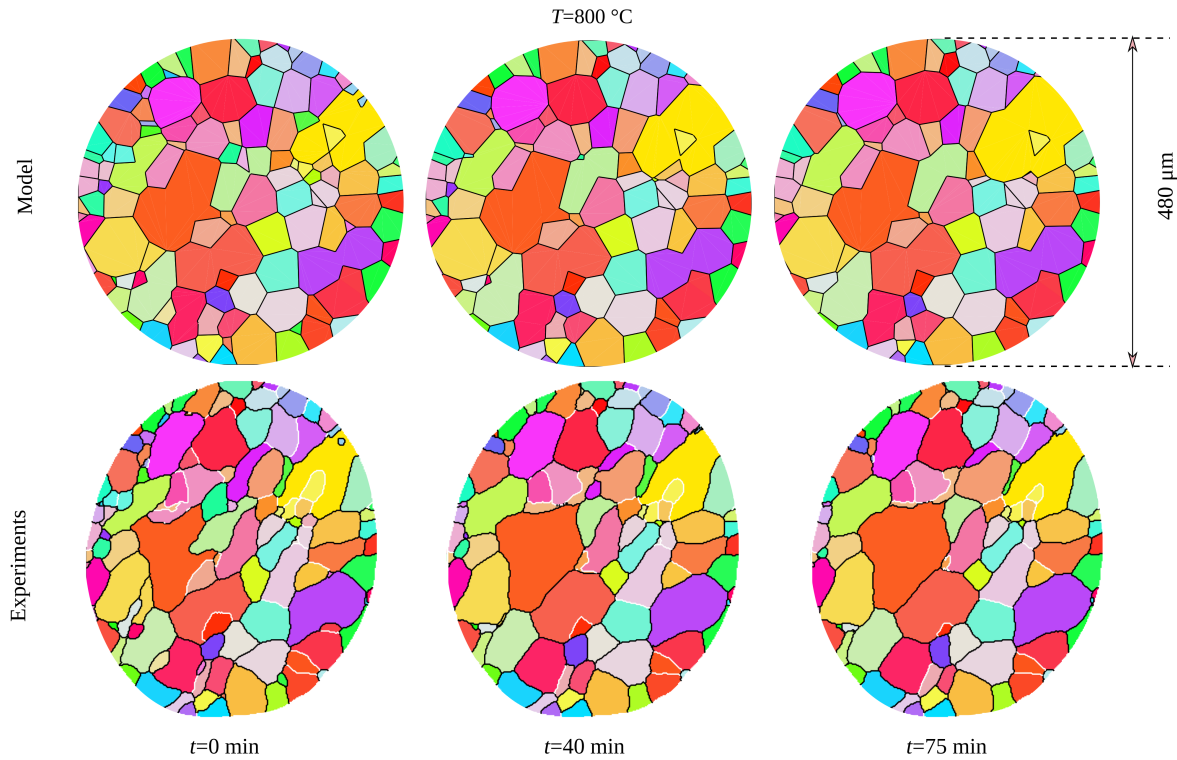


Figure 16: Comparison between the model (top) and experiment (bottom) extracted from [36].

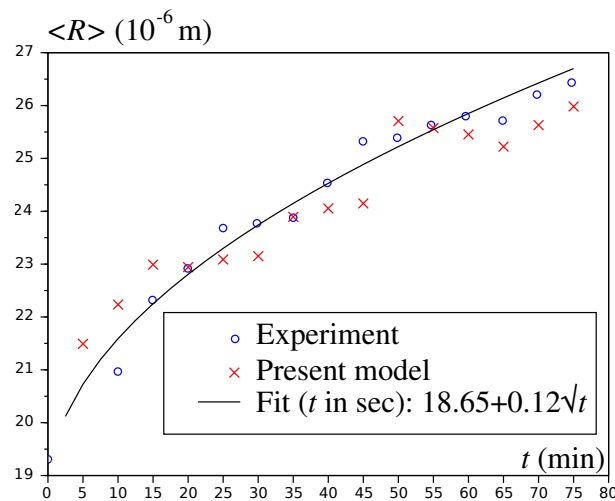


Figure 17: Average equivalent radius $\langle R \rangle$, comparison between the proposed model and the experiment extracted from [36].

7.4. Discussion

In this section, grain statistics are analyzed in more details. The objective is to determine meaningful statistical information that should be considered at the macroscopic scale. Indeed, classical vNM law and Hillert distribution are based only on the average grain size, which is very limited if a specific microstructure is targeted during fabrication or forming processes. In addition, since anisotropic grain growth is considered, BMDs should be captured with sufficient details so that other distributions (e.g., grain size and shape) may be estimated accurately. Four simulations have been performed, with the same initial 2500 grains Voronoi-Laguerre tessellation (see figure 18). Crystallographic orientations have been assigned so that different means and standard deviations of BMDs are obtained, as listed in table 2. The evolution is computed according to condition 2 listed in table 1. The evolution of mean and standard deviation of grain surface distribution (denoted by $\langle S \rangle$ and σ_S) and BMD (denoted by $\langle \Delta\theta \rangle$ and $\sigma_{\Delta\theta}$) are provided respectively in figures 19 and 20. Since anisotropic grain growth is considered, the initial mean misorientation affects the growth rate (see figure 19a). In addition, the initial mean misorientation also affects the standard deviation of size distribution (see figure 19b, comparison between conditions BMD 2 and BMD 3). Thus, grains not only tends to grow in average at different rates according to the mean misorientation, but the distribution also tends to spread at different rates. The evolution of the grain surface distribution also depends on the initial standard deviation of BMD (comparison between conditions BMD 3 and BMD 4). Moreover, significant variations of the mean of BMD are observed in figure 20a and strongly depend on the initial standard deviation (see figure 20b).

Distributions characterizing microstructures (grain size, shape, orientation, misorientation etc.) constitute a very rich information, which cannot be processed for each material points at the macroscopic scale. However, these distributions may be characterized in a simplified way by a measure of central tendency and statistical dispersion (e.g., mean and standard deviation). Previous examples demonstrate that both mean and standard deviation significantly evolve during anisotropic grain growth. Moreover, couplings between different distributions (e.g., size and misorientation) have been obtained. Thus, the macroscopic model that has to be developed in the subsequent paper [2], should involve fully coupled state variables characterizing means and standard deviations of different distributions.

Table 2: BMD: initial condition

Condition	Mean (°)	Standard deviation (°)
BMD 1	≈ 21	≈ 13.5
BMD 2	≈ 21	≈ 10
BMD 3	≈ 12.5	≈ 10
BMD 4	≈ 12.5	≈ 6.5

8. Conclusion

An energetic upscaling strategy has been proposed to model grain growth by considering energetic contributions and dissipated power at various scales. This strategy necessitates to establish a large database of computations at the mesoscopic scale in order to feed a macroscopic model whose state variables represent statistical descriptor of the polycrystal. Thus, a

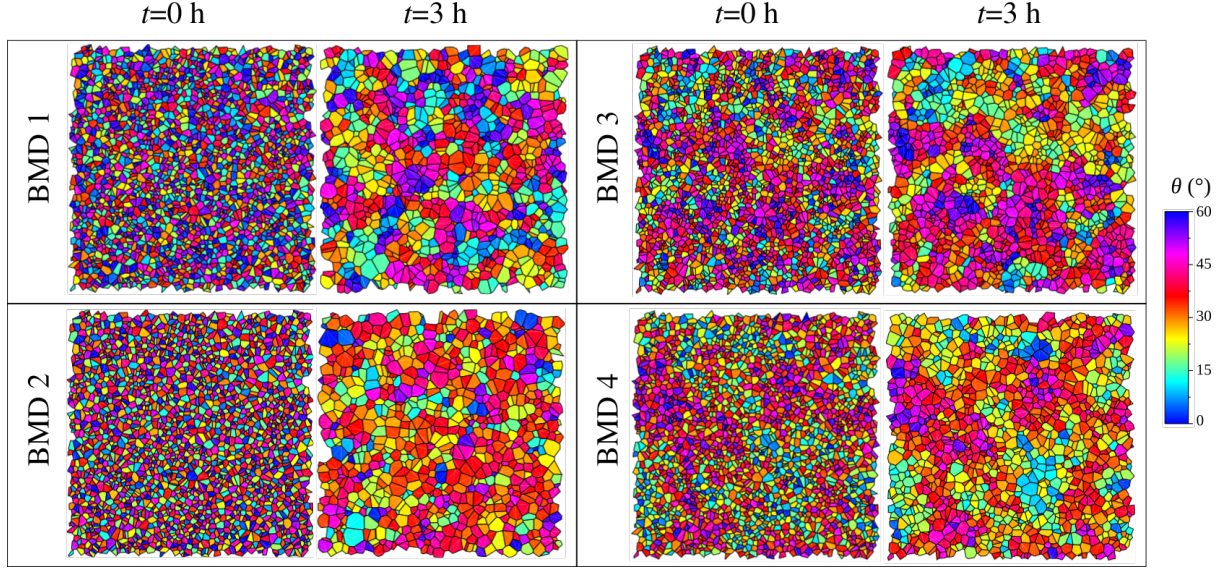


Figure 18: Initial OT and after 3 h evolution at $T = 800^\circ$ for all conditions listed in table 2

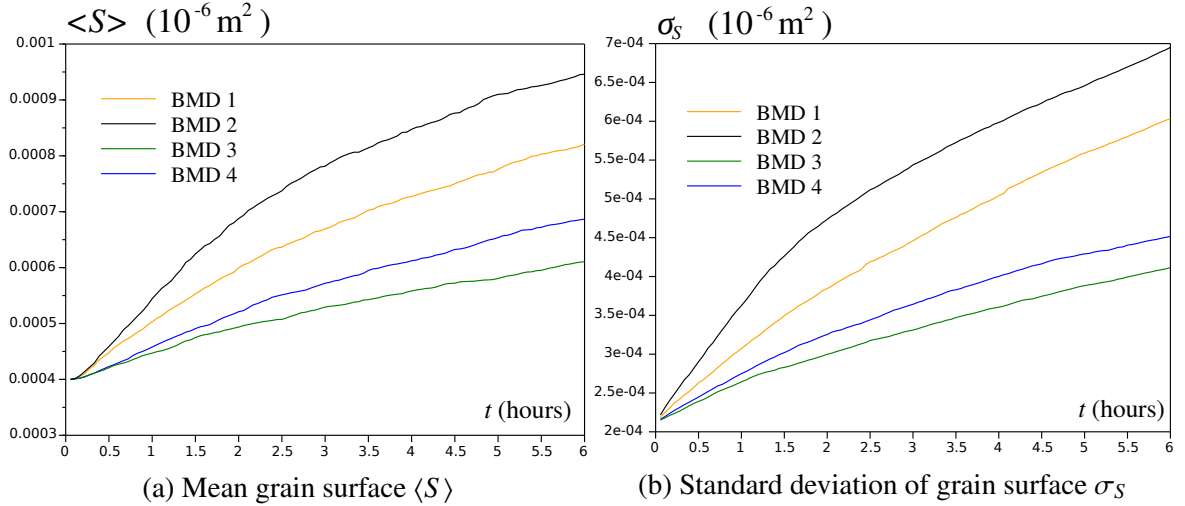


Figure 19: Evolution of grain surface statistics

fast mesoscopic model based on orientated tessellation updating method has been proposed. The space of possible orientated tessellations can be probed by generating a large number of tessellations with various grain statistics and boundary misorientation distributions. To do so, a procedure to assign crystal orientations has been proposed, and relies on a probabilistic approach enabling to approximately fit targeted boundary misorientation distributions. Representative volume elements have been defined so that boundary conditions may be applied, and mass conservation has been verified to be statistically valid if the number of grains is sufficient. The grain boundary energy has been evaluated by molecular dynamics computations and the dissipated power associated to boundary motion has been evaluated. Thus, the total grain boundary energy and total dissipation in the representative volume element has been calculated as the sum of all grain boundary contributions. The mesoscopic evolution law has been derived by maximizing the total dissipation under the constraint of the first and second laws of thermodynamics and mass balance. The present mesoscopic model has been validated for

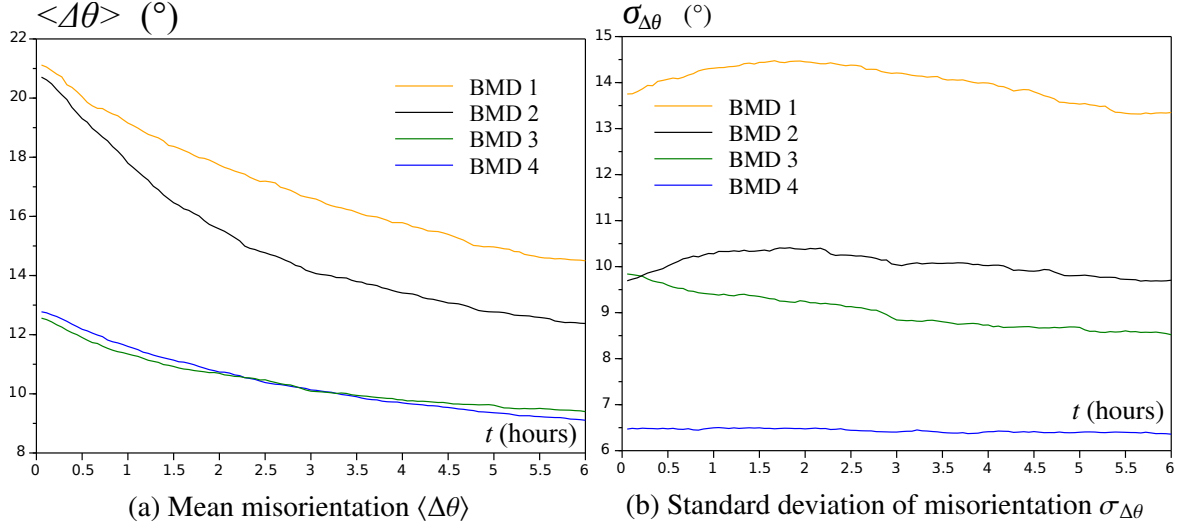


Figure 20: Evolution of misorientation statistics

several conditions by comparing to von Neumann-Mullins law, and classical Hillert distribution. In addition, a good agreement is observed with an annealing experiment conducted on pure iron. The model has been used to analyze the evolution of grain statistics during grain growth, and coupleings between means and standard deviations of various distributions (size, misorientation etc.) have been found necessary to capture grain growth at the macroscopic scale. Thus, the present fast mesoscopic model can be intensively used within framework of the proposed upscaling strategy, and therefore contributes to model detailed grain statistics at very large scales, and tailor microstructures by optimizing fabrication or forming processes.

Appendix A. Geometrical relationships

The gradient $\partial l_{ij}/\partial \mathbf{w}$ is obtained by considering the set of triple junctions:

$$I_3 = \{(i, j, k) \in \{1, \dots, n\}^3, C_i \cap C_j \cap C_k \neq \emptyset\} \quad (\text{A.1})$$

and the angles at the triple junctions denoted by β_{ijk} , where $(i, j, k) \in I_3$ and where the following symmetry rule holds $\beta_{ijk} = \beta_{kji}$. Triple junctions and the effect of weight variation on the length of the GB is presented figure A.21a. From simple geometrical consideration one obtains:

$$\begin{aligned} \dot{l}_{ij} = & \frac{\tan(\beta_{ijk} - \frac{\pi}{2}) + \tan(\beta_{ijm} - \frac{\pi}{2})}{2d_{ij}} \dot{w}_i^* + \frac{\tan(\beta_{jik} - \frac{\pi}{2}) + \tan(\beta_{jim} - \frac{\pi}{2})}{2d_{ij}} \dot{w}_j^* \\ & - \frac{1}{2d_{jk} \cos(\beta_{ijk} - \frac{\pi}{2})} \dot{w}_k^* - \frac{1}{2d_{jm} \cos(\beta_{ijm} - \frac{\pi}{2})} \dot{w}_m^* \end{aligned} \quad (\text{A.2})$$

Moreover:

$$\dot{l}_{ij} = \left(\frac{\partial l_{ij}}{\partial \mathbf{w}} \right) \cdot \dot{\mathbf{w}}^* \quad (\text{A.3})$$

Hence:

$$\frac{\partial l_{ij}}{\partial w_q} = \sum_{p=1}^n \tilde{\delta}_{ijp} \left(\frac{\tan(\beta_{ijp} - \frac{\pi}{2})}{2d_{ij}} \delta_{iq} + \frac{\tan(\beta_{jip} - \frac{\pi}{2})}{2d_{ij}} \delta_{jq} - \frac{\delta_{pq}}{2d_{jp} \cos(\beta_{ijp} - \frac{\pi}{2})} \right) \quad (\text{A.4})$$

where δ_{ij} is the Kronecker symbol and:

$$\tilde{\delta}_{ijk} = \begin{cases} 1 & \text{if } (i, j, k) \in I_3 \\ 0 & \text{if } (i, j, k) \notin I_3 \end{cases} \quad (\text{A.5})$$

The gradient $\partial S / \partial \mathbf{w}$ is obtained by calculating the dimensionless area S_i of a grain i as a

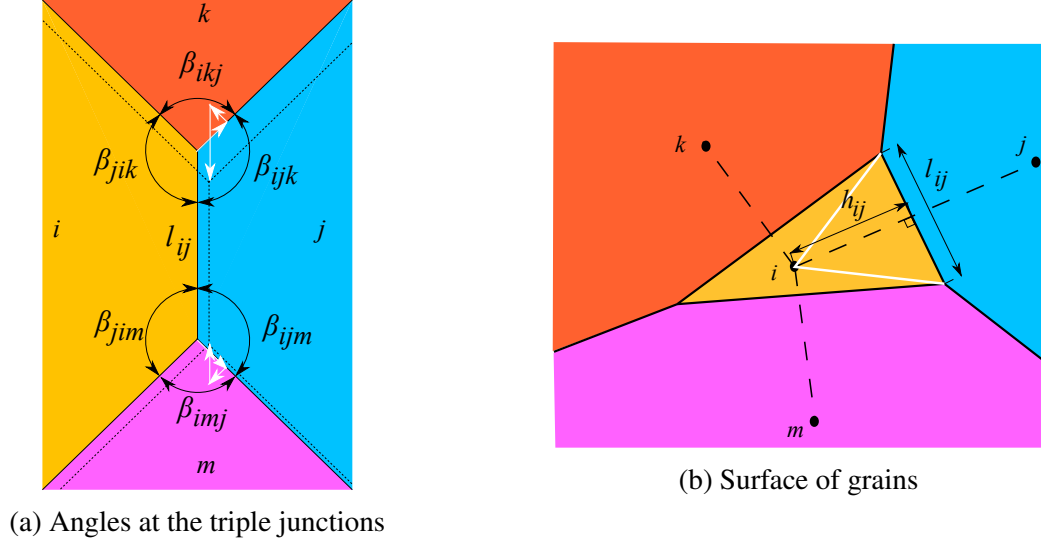


Figure A.21: Geometrical relationship

function of the heights h_{ij} of the triangles joining the seed i and the grain boundaries l_{ij} (where j denotes the neighboring grains), as shown in figure A.21b.

$$S_i = \frac{1}{2} \sum_{j=1}^N \tilde{\delta}_{ij} l_{ij} h_{ij} \quad (\text{A.6})$$

where $\tilde{\delta}_{ij} = 1$ if i and j are neighbors (i.e., $(i, j) \in I_{\text{RVE}}$) and $\tilde{\delta}_{ij} = 0$ otherwise, and the sum is taken over all the grains in the OT because GBs at the edges of the RVE connect grains not belonging to the RVE. The height h_{ij} is obtained by using the definition of the Voronoi-Laguerre tessellation:

$$h_{ij} = \frac{w_i - w_j + d_{ij}^2}{2d_{ij}} \quad (\text{A.7})$$

Hence:

$$\dot{S}_i = \frac{1}{4} \sum_{j=1}^N \frac{\tilde{\delta}_{ij}}{d_{ij}} \left[\dot{l}_{ij} (w_i - w_j + d_{ij}^2) + l_{ij} (\dot{w}_i - \dot{w}_j) \right] \quad (\text{A.8})$$

Moreover:

$$\dot{S}_i = \frac{\partial S_i}{\partial \underline{\mathbf{w}}} \cdot \underline{\dot{\mathbf{w}}} \quad (\text{A.9})$$

Hence:

$$\frac{\partial S_i}{\partial w_q} = \frac{1}{4} \sum_{j=1}^n \frac{\tilde{\delta}_{ij}}{d_{ij}} \left[(w_i - w_j + d_{ij}^2) \frac{\partial l_{ij}}{\partial w_q} + (\delta_{iq} - \delta_{jq}) l_{ij} \right] \quad (\text{A.10})$$

Hence:

$$\frac{\partial S}{\partial w_q} = \frac{1}{4} \sum_{i=1}^n \sum_{j=1}^N \frac{\tilde{\delta}_{ij}}{d_{ij}} \left[(w_i - w_j + d_{ij}^2) \frac{\partial l_{ij}}{\partial w_q} + (\delta_{iq} - \delta_{jq}) l_{ij} \right] \quad (\text{A.11})$$

where the sum on i is taken over grains belonging to the RVE.

Appendix B. Calibration with respect to curvature driven evolution law

The shrinkage of a circular grain in an infinite matrix with a misorientation $\Delta\theta$ is modeled according to the curvature driven evolution law (1). To calibrate the mobility $m(T)$ introduced in (23), the shrinkage of a hexagonal grain is modeled by OTUM as shown in figure B.22. From (A.4) one obtains for the situation defined in figure B.22:

$$\forall j \in \{2, \dots, 7\}, \frac{\partial l_{1j}}{\partial w_1} = \frac{\partial l_{1j}}{\partial w_j} = -\frac{\partial l_{1j}}{\partial w_{j-1}} = -\frac{\partial l_{1j}}{\partial w_{j+1}} = \frac{1}{2\sqrt{3}R} \quad (\text{B.1})$$

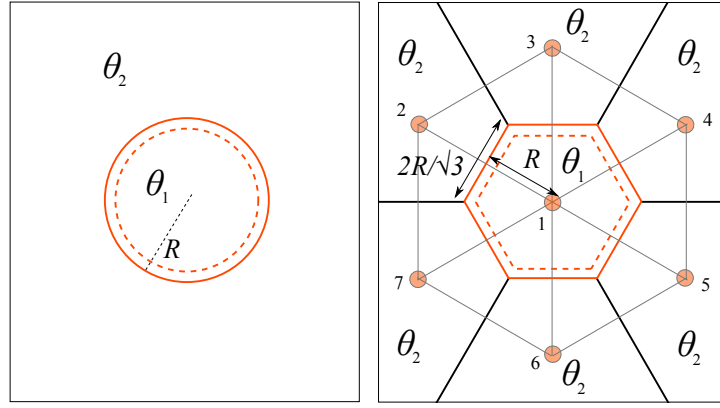


Figure B.22: Circular grain shrinkage in an infinite matrix

The second order tensor χ introduced in (32) reads:

$$\chi = \frac{2R}{\sqrt{3}} \frac{X(\Delta\theta)}{m(T)} \mathbf{I} \quad (\text{B.2})$$

Thus, the second order tensor \mathbf{R} introduced in (37) and its pseudo-inverse \mathbf{M} introduced in (54) are computed. Hence the evolution law (53) for the hexagonal situation can be used to obtain \dot{w}_{meso} , and by using (33) one obtains the inward normal speed according to the proposed model:

$$v_{CD} = \frac{m(T)}{R} \frac{\gamma(T, \Delta\theta)}{X(\Delta\theta)} \quad (\text{B.3})$$

Combining (1) and (B.3) one obtains:

$$m(T) = m_{CD}(T, \Delta\theta) X(\Delta\theta) \quad (\text{B.4})$$

References

- [1] J. Humphreys, G. Rohrer, A. Rollett, *Recrystallization and related annealing phenomena*, Elsevier, 2017. Third edition.
- [2] S. Sakout, D. Weisz-Patrault, A. Ehrlacher, Energetic upscaling strategy for grain growth. II: Probabilistic macroscopic model identified by Bayesian techniques., *Acta Materialia* (2020 (submission)).
- [3] K. Hackl, Generalized standard media and variational principles in classical and finite strain elastoplasticity, *Journal of the Mechanics and Physics of Solids* 45 (1997) 667–688.
- [4] M. A. Miodownik, A review of microstructural computer models used to simulate grain growth and recrystallisation in aluminium alloys, *Journal of Light Metals* 2 (2002) 125–135.
- [5] D. Kandel, E. Domany, Rigorous derivation of domain growth kinetics without conservation laws, *Journal of Statistical Physics* 58 (1990) 685–706.
- [6] E. A. Holm, G. N. Hassold, M. A. Miodownik, On misorientation distribution evolution during anisotropic grain growth, *Acta Materialia* 49 (2001) 2981–2991.
- [7] E. A. Holm, M. A. Miodownik, A. D. Rollett, On abnormal subgrain growth and the origin of recrystallization nuclei, *Acta Materialia* 51 (2003) 2701–2716.
- [8] J. Gruber, H. Miller, T. Hoffmann, G. Rohrer, A. Rollett, Misorientation texture development during grain growth. part i: Simulation and experiment, *Acta Materialia* 57 (2009) 6102–6112.
- [9] L. Zhang, A. D. Rollett, T. Bartel, D. Wu, M. T. Lusk, A calibrated Monte Carlo approach to quantify the impacts of misorientation and different driving forces on texture development, *Acta Materialia* 60 (2012) 1201–1210.
- [10] A. Kuprat, D. George, G. Straub, M. C. Demirel, Modeling microstructure evolution in three dimensions with grain3d and lagrit, *Computational Materials Science* 28 (2003) 199–208.
- [11] J. Gruber, D. C. George, A. P. Kuprat, G. S. Rohrer, A. D. Rollett, Effect of anisotropic grain boundary properties on grain boundary plane distributions during grain growth, *Scripta materialia* 53 (2005) 351–355.
- [12] H. a. Hallberg, Influence of anisotropic grain boundary properties on the evolution of grain boundary character distribution during grain growth a 2d level set study, *Modelling and Simulation in Materials Science and Engineering* 22 (2014) 085005.
- [13] B. Scholtes, R. Boulais-Sinou, A. Settefrati, D. P. Muoz, I. Poitraul, A. Montouchet, N. Bozzolo, M. Bernacki, 3d level set modeling of static recrystallization considering stored energy fields, *Computational Materials Science* 122 (2016) 57–71.

- [14] J. Fausty, N. Bozzolo, M. Bernacki, A 2d level set finite element grain coarsening study with heterogeneous grain boundary energies, *Applied Mathematical Modelling* 78 (2020) 505–518.
- [15] N. Ma, A. Kazaryan, S. Dregia, Y. Wang, Computer simulation of texture evolution during grain growth: effect of boundary properties and initial microstructure, *Acta Materialia* 52 (2004) 3869–3879.
- [16] C. Krill III, L.-Q. Chen, Computer simulation of 3-D grain growth using a phase-field model, *Acta materialia* 50 (2002) 3059–3075.
- [17] L. Vanherpe, N. Moelans, B. Blanpain, S. Vandewalle, Bounding box framework for efficient phase field simulation of grain growth in anisotropic systems, *Computational Materials Science* 50 (2011) 2221–2231.
- [18] G. Abrivard, E. P. Busso, S. Forest, B. Appolaire, Phase field modelling of grain boundary motion driven by curvature and stored energy gradients. part i: theory and numerical implementation, *Philosophical magazine* 92 (2012) 3618–3642.
- [19] G. Abrivard, E. P. Busso, S. Forest, B. Appolaire, Phase field modelling of grain boundary motion driven by curvature and stored energy gradients. part ii: application to recrystallisation, *Philosophical magazine* 92 (2012) 3643–3664.
- [20] K. Chang, N. Moelans, Effect of grain boundary energy anisotropy on highly textured grain structures studied by phase-field simulations, *Acta Materialia* 64 (2014) 443–454.
- [21] M. Upmanyu, D. Srolovitz, L. Shvindlerman, G. Gottstein, Misorientation dependence of intrinsic grain boundary mobility: simulation and experiment, *Acta materialia* 47 (1999) 3901–3914.
- [22] M. Upmanyu, D. Srolovitz, L. Shvindlerman, G. Gottstein, Molecular dynamics simulation of triple junction migration, *Acta materialia* 50 (2002) 1405–1420.
- [23] M. Upmanyu, D. J. Srolovitz, A. Lobkovsky, J. A. Warren, W. Carter, Simultaneous grain boundary migration and grain rotation, *Acta Materialia* 54 (2006) 1707–1719.
- [24] F. Humphreys, Modelling mechanisms and microstructures of recrystallisation, *Materials Science and Technology* 8 (1992) 135–144.
- [25] F. Wakai, N. Enomoto, H. Ogawa, Three-dimensional microstructural evolution in ideal grain growth general statistics, *Acta Materialia* 48 (2000) 1297–1311.
- [26] M. Syha, D. Weygand, A generalized vertex dynamics model for grain growth in three dimensions, *Modelling and Simulation in Materials Science and Engineering* 18 (2009) 015010.
- [27] A. Vondrous, M. Reichardt, B. Nestler, Growth rate distributions for regular two-dimensional grains with ReadShockley grain boundary energy, *Modelling and Simulation in Materials Science and Engineering* 22 (2014) 025014.

- [28] D. Weisz-Patrault, S. Sakout, A. Ehrlacher, Fast simulation of grain growth based on orientated tessellation updating method, *Mechanics & Industry* (2020 (in press)).
- [29] R. Quey, P. Dawson, F. Barbe, Large-scale 3d random polycrystals for the finite element method: Generation, meshing and remeshing, *Computer Methods in Applied Mechanics and Engineering* 200 (2011) 1729–1745.
- [30] H. Telley, T. M. Liebling, A. Mocellin, F. Righetti, Simulating and modelling grain growth as the motion of a weighted voronoi diagram, in: *Materials Science Forum*, volume 94, Trans Tech Publ, 1992, pp. 301–306.
- [31] E. Schüle, A justification of the hillert distribution by spatial grain growth simulation performed by modifications of laguerre tessellations, *Computational materials science* 5 (1996) 277–285.
- [32] M. Hillert, On the theory of normal and abnormal grain growth, *Acta metallurgica* 13 (1965) 227–238.
- [33] A. L. Cruz-Fabiano, R. Logé, M. Bernacki, Assessment of simplified 2d grain growth models from numerical experiments based on a level set framework, *Computational materials science* 92 (2014) 305–312.
- [34] J. Von Neumann, *Metal interfaces*, American Society for Metals, Cleveland 108 (1952).
- [35] D. Moldovan, D. Wolf, S. Phillpot, A. Haslam, Mesoscopic simulation of two-dimensional grain growth with anisotropic grain-boundary properties, *Philosophical Magazine A* 82 (2002) 1271–1297.
- [36] J. Zhang, Y. Zhang, W. Ludwig, D. Rowenhorst, P. W. Voorhees, H. F. Poulsen, Three-dimensional grain growth in pure iron. part i. statistics on the grain level, *Acta Materialia* 156 (2018) 76–85.
- [37] J. Mackenzie, Second paper on statistics associated with the random disorientation of cubes, *Biometrika* 45 (1958) 229–240.
- [38] M. Miodownik, A. Godfrey, E. Holm, D. Hughes, On boundary misorientation distribution functions and how to incorporate them into three-dimensional models of microstructural evolution, *Acta materialia* 47 (1999) 2661–2668.
- [39] M. Groeber, S. Ghosh, M. D. Uchic, D. M. Dimiduk, A framework for automated analysis and simulation of 3d polycrystalline microstructures. part 2: Synthetic structure generation, *Acta Materialia* 56 (2008) 1274–1287.
- [40] G. S. Rohrer, Grain boundary energy anisotropy: a review, *Journal of materials science* 46 (2011) 5881–5895.
- [41] W. T. Read, W. Shockley, Dislocation models of crystal grain boundaries, *Physical review* 78 (1950) 275.
- [42] D. Wolf, Structure-energy correlation for grain boundaries in fcc metals. boundaries on the (111) and (100) planes, *Acta metallurgica* 37 (1989) 1983–1993.

- [43] D. Wolf, Structure-energy correlation for grain boundaries in fcc metalsii. boundaries on the (110) and (113) planes, *Acta Metallurgica* 37 (1989) 2823–2833.
- [44] D. Wolf, Structure-energy correlation for grain boundaries in fcc metalsiii. symmetrical tilt boundaries, *Acta metallurgica et materialia* 38 (1990) 781–790.
- [45] D. Wolf, Structure-energy correlation for grain boundaries in fcc metalsiv. asymmetrical twist (general) boundaries, *Acta Metallurgica et Materialia* 38 (1990) 791–798.
- [46] M. Tschopp, D. McDowell, Asymmetric tilt grain boundary structure and energy in copper and aluminium, *Philosophical Magazine* 87 (2007) 3871–3892.
- [47] M. A. Tschopp, S. P. Coleman, D. L. McDowell, Symmetric and asymmetric tilt grain boundary structure and energy in cu and al (and transferability to other fcc metals), *Integrating Materials and Manufacturing Innovation* 4 (2015) 11.
- [48] S. Ratanaphan, D. L. Olmsted, V. V. Bulatov, E. A. Holm, A. D. Rollett, G. S. Rohrer, Grain boundary energies in body-centered cubic metals, *Acta Materialia* 88 (2015) 346–354.
- [49] P. Van Beers, V. Kouznetsova, M. Geers, M. Tschopp, D. McDowell, A multiscale model of grain boundary structure and energy: From atomistics to a continuum description, *Acta Materialia* 82 (2015) 513–529.
- [50] V. V. Bulatov, B. W. Reed, M. Kumar, Grain boundary energy function for fcc metals, *Acta Materialia* 65 (2014) 161–175.
- [51] S. Plimpton, Fast parallel algorithms for short-range molecular dynamics, *Journal of computational physics* 117 (1995) 1–19.
- [52] H. Chamati, N. Papanicolaou, Y. Mishin, D. Papaconstantopoulos, Embedded-atom potential for fe and its application to self-diffusion on fe (1 0 0), *Surface Science* 600 (2006) 1793–1803.
- [53] E. B. Tadmor, R. S. Elliott, J. P. Sethna, R. E. Miller, C. A. Becker, The potential of atomistic simulations and the knowledgebase of interatomic models, *Jom* 63 (2011) 17.
- [54] D. Wolf, A Read-Shockley model for high-angle grain boundaries, *Scripta Metallurgica* 23 (1989) 1713–1718.
- [55] T. Cheng, D. Fang, Y. Yang, The temperature dependence of grain boundary free energy of solids, *Journal of Applied Physics* 123 (2018) 085902.
- [56] A. Kagawa, T. Okamoto, H. Matsumoto, Young's modulus and thermal expansion of pure iron-cementite alloy castings, *Acta Metallurgica* 35 (1987) 797–803.
- [57] M. Brocato, A. Ehrlacher, P. Tamagny, Dtermination de la dissipation caractéristique dans la propagation d'un front de recristallisation, *Comptes Rendus de l'Académie des Sciences-Series IIB-Mechanics-Physics-Astronomy* 327 (1999) 179–184.

- [58] M. Brocato, A. Ehrlacher, P. Tamagny, Stability of discontinuities in polycrystals, *Waves and Stability in Continuous Media* (1999) 57.
- [59] F. Humphreys, A unified theory of recovery, recrystallization and grain growth, based on the stability and growth of cellular microstructures. the basic model, *Acta Materialia* 45 (1997) 4231–4240.
- [60] F. Humphreys, Stability and growth of grain and subgrain structures in two-phase materials, in: *Third international conference in grain growth in polycrystalline materials*, volume 1, Minerals, Metals and Materials Society, 1998, pp. 13–22.
- [61] K. Hackl, F. D. Fischer, On the relation between the principle of maximum dissipation and inelastic evolution given by dissipation potentials, *Proceedings of the Royal Society A: Mathematical, Physical and Engineering Sciences* 464 (2007) 117–132.
- [62] Scilab, Scilab 6.0.0: Free and Open Source software for numerical computation v, Scilab Enterprises, Orsay, France (2019).
- [63] W. W. Mullins, Two-dimensional motion of idealized grain boundaries, *Journal of Applied Physics* 27 (1956) 900–904.